Physicochemical Characterization and Source Apportionment of Arctic Ice Nucleating Particles Observed in Ny-Ålesund in Autumn 2019

Guangyu Li[1], Elise K. Wilbourn[2], Zezhen Cheng[3], Jörg Wieder[1,*], Allison Fagerson[4], Jan Henneberger[1], Ghislain Motos[5], Rita Traversi[6,7], Sarah D. Brooks[4], Mauro Mazzola[7], Swarup China[3], Athanasios Nenes[5,8], Ulrike Lohmann[1], Naruki Hiranuma[2], and Zamin A. Kanji[1]

[1]Institute for Atmospheric and Climate Science, ETH Zurich, Switzerland
[2]Department of Life, Earth and Environmental Sciences, West Texas A&M University, Canyon, Texas, USA
[3]Environmental Molecular Sciences Laboratory, Pacific Northwest National Laboratory (PNNL), Richland, Washington, USA
[4]Department of Atmospheric Sciences, Texas A&M University, Texas, USA
[5]Laboratory of Atmospheric Processes and their Impacts, School of Architecture, Civil and Environmental Engineering, Ecole Polytechnique Fédérale de Lausanne (EPFL), Lausanne, Switzerland
[6]Department of Chemistry "Ugo Schiff", University of Florence, Sesto Fiorentino, 50019 Florence, Italy
[7]Institute of Polar Sciences of the National Research Council of Italy (ISP-CNR), Venice, Italy
[8]Institute of Chemical Engineering Sciences, Foundation for Research and Technology Hellas, Patras, Greece
*now at: femtoG AG, Zurich, Switzerland

Correspondence: Guangyu Li (guangyu.li@env.ethz.ch) and Zamin A. Kanji (zamin.kanji@env.ethz.ch)

Abstract.

Ice nucleating particles (INPs) initiate primary ice formation in Arctic mixed-phase clouds (MPCs), altering cloud radiative properties and modulating precipitation. For atmospheric INPs, the complexity of their spatiotemporal variations, heterogeneous sources and evolution via intricate atmospheric interactions challenge the understanding of their impact on microphysical processes in Arctic MPCs and induce an uncertain representation in climate models. In this work, we performed a comprehensive analysis of atmospheric aerosols at the Arctic coastal site in Ny-Ålesund (Svalbard, Norway) from October to November 2019, including their ice nucleation ability, physicochemical properties and potential sources. Overall, INP concentrations (N_{INP}) during the observation season were approximately up to three orders of magnitude lower compared to the global average, with several samples showing degradation of N_{INP} after heat treatment, implying the presence of proteinaceous INPs. Particle fluorescence was substantially associated with INP concentrations at warmer ice nucleation temperatures, indicating that in the far-reaching Arctic, aerosols of biogenic origin throughout the snow- and ice-free season may serve as important INP sources. In addition, case studies revealed the links between elevated N_{INP} to heat-lability, fluorescence, high wind speeds originating from the ocean, augmented concentration of coarse-mode particles and abundant organics. Backward trajectory analysis demonstrated a potential connection between high-latitude dust sources and high INP concentrations, while prolonged air mass history over the ice pack was identified for most scant INP cases. The combination of the above analyses demonstrates the abundance, physicochemical properties and potential sources of INPs in the Arctic are highly variable despite its remote location.

1   Introduction

Arctic regions are extremely sensitive to climate change. Over the past few decades, it has been reported that the anthropogenic warming in the Arctic is two to three times faster than the global average (Forster et al., 2021; Wendisch et al., 2019; Serreze and Barry, 2011), a phenomenon commonly known as Arctic amplification. Satellite observations have revealed a considerable retreat of Arctic sea ice extent in all seasons (Stroeve et al., 2012; Serreze et al., 2007), which is identified as one of the principal drivers of Arctic amplification given the positive surface-albedo feedback (Screen and Simmonds, 2010; Hall, 2004). Modeling studies (Pithan and Mauritsen, 2014; Graversen and Wang, 2009; Hall, 2004) have also verified Arctic amplification in the absence of surface-albedo feedback. Additionally, other feedbacks are also suggested as important contributors to Arctic amplification, including atmospheric and oceanic heat transport from the mid-latitudes (Spielhagen et al., 2011), the greenhouse effect of additional water vapor (Graversen and Wang, 2009), lapse-rate associated with the vertical structure of warming (Bintanja et al., 2012) and cloud feedbacks (Korolev et al., 2017; Vavrus, 2004; Intrieri et al., 2002). Cloud feedbacks are nontrivial to Arctic amplification given the ubiquity of clouds and their potential to affect the radiative balance at both the surface and the top of the atmosphere. However, accurate quantification and prediction of cloud-induced feedbacks to climate change remain challenging due to the rudimentary understanding of aerosol-cloud interactions and inadequate model representations (Forster et al., 2021; Schmale et al., 2021; Murray et al., 2021), particularly in the remote Arctic.

Low-level mixed-phase clouds (MPCs), composed of a mixture of ice and supercooled liquid water, play a critical role in the energy budget given their spatiotemporal prevalence in the Arctic (Forster et al., 2021; Korolev et al., 2017; Morrison et al., 2012). The phase partitioning of hydrometeors within the MPCs is an essential microphysical process that intrinsically drives the cloud feedback because more liquid water and fewer ice crystals (i.e., the trend in the warming future) are associated with increased cloud albedo and diminished downwelling short-wave radiation, leading to a negative cloud-phase feedback to climate change (Lohmann and Neubauer, 2018; Storelvmo, 2017). In MPCs, where the ~~temperatures are~~ temperature is higher than the onset ~~threshold~~ of homogeneous freezing (at approximately -38 °C)for cloud droplet relevant sizes, primary ice formation can only be triggered with the aid of a small subset of aerosol particles termed ice nucleating particles (INPs, e.g., Kanji et al., 2017; Vali et al., 2015). Immersion freezing, a heterogeneous freezing process where INPs become immersed in a dilute aqueous solution through the activation of cloud droplets followed by catalyzing freezing from within (Vali et al., 2015), is considered the most important freezing mode in the MPCs (Kanji et al., 2017; Hande and Hoose, 2017; Westbrook and Illingworth, 2013) and will be the focus of this study. Frequently, secondary ice production increases ice crystal concentrations to several orders of magnitude higher than the INP concentration (Korolev et al., 2020), but also cases with ice crystal number concentrations limited by the available INPs were observed in the Arctic (Pasquier et al., 2022b). Despite the extraordinary paucity of INPs in the troposphere and that at -15 °C, approximately 1 in 10^5 to 10^6 aerosol particles can act as an INP (e.g., Kanji et al., 2017; Petters and Wright, 2015), their type, abundance and variability can indirectly affect the climate by altering the microphysical and radiative properties of MPCs (e.g., DeMott et al., 2010; Lohmann, 2002). For instance, cloud-resolving modeling studies revealed that the liquid and ice water path (Eirund et al., 2019), atmospheric stability (Jiang et al., 2000; Harrington et al., 1999) and precipitation (Harrington and Olsson, 2001) in the Arctic MPCs respond sensitively to INP perturbations in abundance and

efficiency, and the responses were dominant over altering the cloud condensation nuclei (CCN) concentrations (Solomon et al., 2018). In addition, the slope of INP concentration versus ice nucleation temperature (i.e., INP efficiency) can influence the development and radiative forcing of convective clouds (Hawker et al., 2021), and with relatively low abundance in the Arctic,

55 enhanced Arctic amplification was simulated given larger and fewer ice particles in MPCs (Tan and Storelvmo, 2019). Moreover, modeling studies (Hines et al., 2021; Vignon et al., 2021; Vergara-Temprado et al., 2018) produced more realistic cloud phase separations with an adjusted microphysics scheme that better represented heterogeneous nucleation processes. Therefore, further constraints on the role of INPs and robust representations in the cloud microphysics parameterizations in climate models are of vital importance to accurately capture the cloud feedback related to Arctic amplification.

60 A variety of aerosols of both terrestrial and marine origin ~~display a range of activities as INPs~~ in the Arctic can act as INPs in the MPC temperature regime. Mineral dust particles can typically act as INPs at temperatures below approximately -15 °C (Kanji et al., 2017; Hoose and Möhler, 2012; Murray et al., 2012). In the Arctic, mineral dust emitted from high latitudes, e.g., from the glacial outwash plains ~~(Tobo et al., 2019) and deserts from~~ in Svalbard (Tobo et al., 2019), from deserts in Iceland (Sanchez-Marroquin et al., 2020), ~~is a significant terrestrial source of INPs in the Arctic. Mineral dust particles can typically act~~

65 ~~as INPs in MPCs regime at temperatures below approximately -15 °C (Kanji et al., 2017; Hoose and Möhler, 2012; Murray et al., 2012)~~ ~~,~~ or dust originating from long-range transport (Vergara-Temprado et al., 2017) are significant terrestrial sources of INPs. In contrast, biological INPs ~~tend to~~ favor heterogeneous ice nucleation at relatively warmer temperatures ~~of~~ above approximately -15 °C (Murray et al., 2012)~~, and their sources~~ . Their sources in the Arctic can stem from land, e.g., vegetation (Conen et al., 2016), ~~sediments from runoff~~ runoff from watersheds (Tobo et al., 2019) and thawing permafrost ~~(Creamean et al., 2020)~~

70 (Barry et al., 2023; Creamean et al., 2020) or from the ocean, e.g., sea spray aerosols (SSA) (Irish et al., 2017; DeMott et al., 2016; Wilson et al., 2015), phytoplankton (Ickes et al., 2020; Hartmann et al., 2020; Creamean et al., 2019) and ~~bacteria~~ bacterial productivity (Šantl Temkiv et al., 2019). In addition to the INP sources originating from the vicinity of the measurement sites in the local Arctic, the remote effect of INP emissions from mid- to low-latitudes and long-range transport cannot be neglected ~~(Schmale et al., 2021; Vergara-Temprado et al., 2017)~~(Schmale et al., 2021). In deterministic INP param-

75 eterizations, the magnitude of the cloud-phase-related feedback relies on the efficiencies of INPs due to their dependency on nucleation temperatures for different INP species (Murray et al., 2021; Hawker et al., 2021).

In this study, we aim to improve our understanding of the abundance, variability, sources, physicochemical properties and impacting factors of INPs in the Arctic based on field measurement data. We introduce the campaign information, experimental setup and ~~instrumentations~~ different INP instrumentation in Section 2. An overview of ambient INP measurements and charac-

80 terization is presented and discussed in Sections 3.1 and 3.2, respectively, and several special case studies are demonstrated in Section 3.3. Section 4 highlights the conclusions from this study and suggests potential implications for the changing climate.

2 Methods

2.1 Measurement location and experimental setup

The measurement campaign of ambient INP and aerosol properties was a part of the Ny-Ålesund AeroSol Cloud ExperimeNT
(NASCENT) campaign (Pasquier et al., 2022a) from October to November 2019 at Ny-Ålesund (78.9 °N, 11.9 °E). Ny-Ålesund
is located on the western coast of the Svalbard Archipelago (Fig. ~~1[a]~~1 a). Ambient INP and aerosol measurements were conducted at two locations; in an aerosol container ~~and Gruvebadet (GVB)~~ (78.923 °N, 11.921 °E) and at Gruvebadet observatory
station ~~(Fig. 1[b]). The atmospheric container was located at the southern edge of Ny-Ålesund town and was approximately~~
~~600 m from the shore of Kongsfjorden. GVB observatory station is located about 1 km south-west from Ny-Ålesund town and~~
~~is approximately 49 m a.s.l.~~ GVB, 78.918 °N, 11.894 °E. See Fig. 1 b). Local sources of pollution have a ~~minimal~~ limited influence on the measurement sites ~~given the prevailing southeasterly and southwesterly winds during the period of measurement~~
~~(Pasquier et al., 2022a).~~ during the measurement period, given the predominant southeasterly wind at the aerosol container and
prevailing southwesterly winds close to the GVB observatory station (see detailed wind pattern in Fig. 1 b).

A flow diagram of the instrument setup is shown in Fig. 2. In the aerosol container, the aerosol flow was sampled through
a total aerosol inlet mounted outside of the container, which was about 4.5 m above the ground. The inlet had an upper cut-off threshold of approximately 40 μm (Li et al., 2022) and was heated to a maximum of 40 °C to avoid clogging and frost
build-up in the sampling line. The evaporation of volatile compounds in the aerosols cannot be excluded. Subsequently, the
aerosol flow was directed into different branches of aerosol and INP instruments (for detailed flow configurations, see Li et al.,
2022). The aerosol samples collected offline by the impinger were later subject to INP measurement via the DRoplet Ice
Nuclei Counter Zurich (DRINCZ, David et al., 2019) and chemical composition analyses using computer-controlled scanning
electron microscopy with energy-dispersive X-ray spectroscopy (CCSEM/EDX) and Raman microspectroscopy. At the GVB
observatory, ambient INPs were analyzed using different offline techniques. Aerosol particles for analysis with DRINCZ were
collected onto the 47 mm polycarbonate membrane filter (Whatman, 0.4 μm pore size) during 8-hour intervals using a low-volume aerosol sampler (LVS, DPA14, Digitel) coupled with a PM_{10} inlet. The height of the inlet was approximately 5 m
a.g.l., and the operating flow rate was 38.3 L min^{-1}. Aerosols for the West Texas Cryogenic Refrigerator Applied to Freezing
Test (WT-CRAFT) analysis were collected using 47 mm polycarbonate membrane filters (Whatman, 0.2 μm pore size) during
4-day intervals (one exception was a 3-day sample started on 27 October 2019) from a central total suspended particulate
(TSP) inlet with a critical-orifice-controlled sampling flow rate of 3.5 std L min^{-1} (for a detailed setup see Rinaldi et al., 2021).
Additionally, the aerosol properties were also monitored at the GVB observatory, including particle size distribution, black
carbon, and chemical compositions. The descriptions of instruments measuring INPs, aerosol physicochemical properties and
meteorological conditions are given below.

2.2 INP sampling and measurement techniques

To investigate the ambient INP concentrations in immersion-freezing mode, we used different INP sampling and measurement
instruments introduced in the following subsections, which provide a large range of sampled particle sizes, time resolutions,
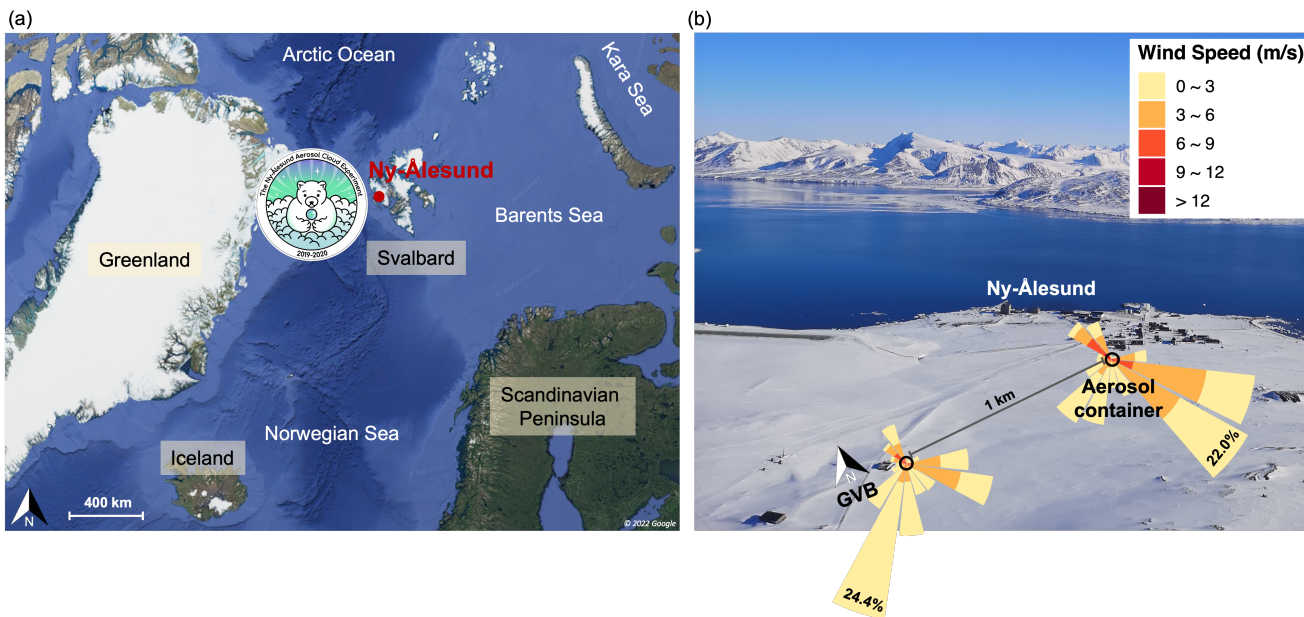
Figure 1. (a) Geographic location of the ~~sampling stations~~ 2019 NASCENT campaign in Ny-Ålesund, Svalbard. ~~The NASCENT campaign logo is shown in (a~~b) ~~. The photo~~ Location of measurement stations in Ny-Ålesund (~~b~~photo taken in mid-October 2019). The atmospheric container was ~~taken~~ located at the ~~mountain Zeppelin~~ southern edge of Ny-Ålesund town and was approximately 600 m from the shore of Kongsfjorden. GVB observatory station is located about 1 km west of Ny-Ålesund town and is approximately 49 m a.s.l. The frequency of occurrence in ~~mid-October 2019.~~wind direction and speed during the 2019 NASCENT campaign are shown for the GVB station and aerosol container. The colored bars of wind roses provide the frequency of occurrence, with the value of the frequency of occurrence of the most likely wind direction displayed at the longest bars.

freezing temperatures, and hence different INP detection limits (see Table 1). In particular, the droplet-freezing techniques (see Sections 2.2.1 and 2.2.2) have different limits of detection (LOD) due to the different droplet sizes and numbers in the experimental setup.

2.2.1 DRINCZ

INP concentrations (N_{INP}) were measured using different offline and online methods. In the aerosol container, ambient aerosols were collected into the ultrapure water (W4502-1L, Sigma-Aldrich) using the high flow-rate impinger (Coriolis® µ, Bertin Instruments, lower limit cut-off size of 0.5 µm) at a flow rate of 300 L min⁻¹ for 1 h. Additional ultrapure water (W4502-1L, Sigma-Aldrich) was constantly supplied to the sampling container via a refilling system during the operation of the impinger in order to compensate for the evaporation losses. The INP analysis for impinger samples was conducted onsite directly after the sample collection. Aerosol filters collected using the PM_{10} inlet at the GVB observatory were analyzed for N_{INP} after the campaign in the laboratory back at ETH after frozen storage and transport at -20 °C. To determine N_{INP}, membrane filters
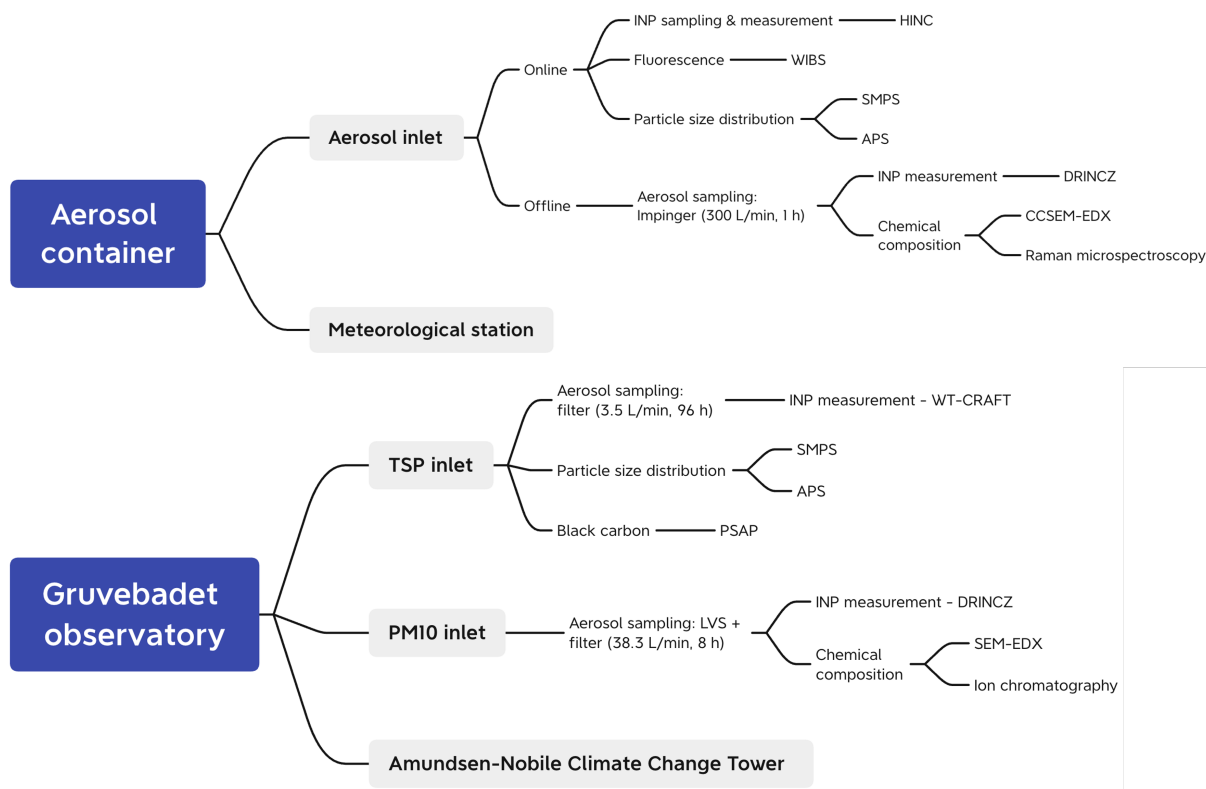
Figure 2. Schematic of the experimental setup in Ny-Ålesund at the aerosol container and Gruvebadet (GVB) observatory. Online means the analytical instruments with real-time aerosol sampling and monitoring, and offline denotes the instruments/devices that collect samples and take post-measurements separately. The sampling flow rates and duration are shown in the parentheses for aerosol sampling instruments. Acronyms meanings: Horizontal Ice Nucleation Chamber (HINC), Wideband Integrated Bioaerosol Sensor (WIBS), Scanning Mobility Particle Sizer (SMPS), Aerodynamic Particle Sizer (APS), DRoplet Ice Nuclei Counter Zurich (DRINCZ), Computer-Controlled Scanning Electron Microscopy with Energy-Dispersive X-ray spectroscopy (CCSEM/EDX), West Texas Cryogenic Refrigerator Applied to Freezing Test (WT-CRAFT) system, particle soot absorption photometer (PSAP) and Low Volume Sampler (LVS).

were immersed in 15 mL of ultrapure water (W4502-1L, Sigma-Aldrich) and agitated using a sonicator to extract the particles into the water. During October and November 2019, a total of 137 and 77 samples were collected by the impinger and PM_{10} filters ~~respectively for immersion mode~~ , respectively, for immersion-mode N_{INP} analysis in DRINCZ (David et al., 2019). Each sample was pipetted into a sealed Polymerase Chain Reaction (PCR) tray with 96 aliquots of 50 µL and cooled in an ethanol bath at 1 °C min^{-1}. During the cooling phase, a camera placed above the bath captures images of the cooling state of the PCR tray and the bath temperature was monitored. From the variation in optical brightness of an aliquot between subsequent images, the freezing temperature of the aliquots was determined. INP concentrations are derived by using the impinger flow rate and volume of an aliquot (see details in David et al., 2019). We calculated N_{INP} at each integer temperature based on (Vali, 1971, 2019):

$$N_{\mathrm{INP}}(T) = -\frac{\ln\left[1 - \dfrac{N_{\mathrm{frz}}(T)}{N_{\mathrm{tot}}}\right]}{V_{\mathrm{a}}} \cdot \frac{V_{\mathrm{liquid}}}{Q_{\mathrm{sample}} \cdot t_{\mathrm{sample}}} \cdot DF \tag{1}$$

where $N_{\mathrm{frz}}(T)$ is the number of frozen aliquots at temperature T, N_{tot} is the total number of aliquots (N_{tot} = 96), V_{a} is the volume of an individual aliquot (V_{a} = 50 µL), V_{liquid} is the volume of sampling liquid (15 mL for impinger), Q_{sample} is the sampling flow rate (300 L min^{-1} for impinger) and t_{sample} is the sampling time (1 h for impinger). DF is the dilution factor, which was applied to quantify the dilutions for some highly IN-active samples. Diluted and non-diluted scans were combined using the methodology provided in Wieder et al. (2022) for these samples. N_{INP} of each sample derived from above were corrected for the background of blank samples based on the methods in David et al. (2019) and Li et al. (2022). For impinger samples, in order to account for contamination from the refilling system and the sampling substrate, blank samples were collected and analyzed every three days during the campaign by adding the same amount of ultrapure water for samples (15 mL) to the sampling container using the refilling system. Concerning PM$_{10}$ filter samples, empty filters were taken onsite and reserved in the filter holders for the same duration as for the sampling stage before being stored, processed and analyzed for background INP concentrations. According to Vali (2019), all field samples were corrected for the background by subtracting the differential INP spectrum of the corresponding blanks from that of the original samples. Based on the ~~limit of detection (LOD)~~ LOD of DRINCZ and purity of the nano-pure water, the highest temperature for N_{INP} detection was approximately -5 °C (around which the instrument is not sensitive enough to detect the low concentrations), and the lowest temperature at which ice nucleation could be reliably reported was -22 °C (below which N_{INP} are usually closed to the background concentrations), with the overall uncertainty of the reported freezing temperature of a well of ±0.9 °C (David et al., 2019).

2.2.2 WT-CRAFT

The WT-CRAFT system, a replica of the Cryogenic Refrigerator Applied to Freezing Test (CRAFT) system (Tobo, 2016), which was used to ~~estimate~~ measure N_{INP} in a unit volume of air for aerosol particles collected at the GVB observatory. With a detection capability of > 0.003 INP std L^{-1} of air, N_{INP} was assessed for a total of seven samples in the temperature range of approximately ~~-25~~ -30 °C to 0 °C, with a systematic uncertainty in freezing temperature of ±0.5 °C (Vepuri et al., 2021). The background contribution may be substantial for the WT-CRAFT N_{INP} data measured below -25 °C. Alternatively, the 95 % confidence interval can represent an experimental uncertainty in the estimated N_{INP} for each measured data point (Rinaldi et al., 2021). All analyses were completed within 1 year after collecting the samples, and the samples were stored in a fridge (4 °C) before commencing the analysis.

For each experiment, the freezing properties of 70 solution droplets (3 µL each) placed on a hydrophobic Vaseline layer were assessed with a cooling rate of 1 °C min^{-1}. A cumulative number of unfrozen droplets were counted for every 0.5 °C based on the color contrast shift in the off-the-shelf video recording camera. If the freezing temperature was not obvious for any droplets, the image analysis was performed using ImageJ software to determine the temperature of phase change. Using

the same Equations. 1, N_{INP} of the samples were estimated as a function of T, where $N_{tot} = 70$, $V_a = 3$ μL, and V_{liquid}, Q_{sample} and t_{sample} depend on the individual samples.

Prior to each WT-CRAFT experiment, particles on an individual filter sample were suspended in a known volume of ultrapure high-performance liquid chromatography (HPLC) grade water. The HPLC water volume was determined for the third frozen droplet to correspond to 0.003 INP L^{-1} according to Equation. 1. It is noteworthy that we limited our WT-CRAFT data analysis to the third frozen droplet to eliminate any uncontrollable artifacts in our WT-CRAFT data (Hiranuma et al., 2019). Because of the negligible background freezing contribution of the field blank filter at -25 °C (i.e., < 3 %), we did not apply any background corrections to our N_{INP} data. Otherwise, we followed the exact same protocols described in Rinaldi et al. (2021) for our suspension generation and dilution.

2.2.3 HINC

To complement the INP measurements at colder temperatures, we sampled and measured N_{INP} with HINC (Lacher et al., 2017), a continuous flow diffusion chamber. HINC was operated at T = -30 °C ($\pm$ 0.4 °C) and relative humidity with respect to water RH_w = 104 % ($\pm$ 1.5 %), representative for ice nucleation in immersion and condensation modes. The detailed experimental configuration of HINC can be found in ~~Fig. 2 of~~ Li et al. (2022). With a size threshold of 5 μm derived from the water droplet survival test (Lacher et al., 2017) at the designed experimental conditions, we were able to distinguish the ice crystals from water droplets during the sampling phase. To account for ~~frost particles that~~ ice particles emitted from frost build-up, which can be misidentified as INPs when detaching from the inner surface, we applied a routine of filtered air measurements (5 min) before and after each sampling interval (15 min) to determine the background count of ice particles and the ~~limit of detection~~ LOD based on Poisson statistics. Subsequently, N_{INP} was calculated by subtracting ice particle concentrations during the background interval from that during the sampling interval (see detailed calculations in Lacher et al., 2017). During the field campaign between October and November 2019, we reported 135 INP concentrations from HINC measurements that were higher than the ~~limit of detection of~~ LOD of the instrument out of a total of 348 observations. In other words, the 135 INP concentration data points have a significance level of 68.3 % and were more reliable for extrapolation due to the limitation of the instrument at the measurement conditions.

~~Using a combination of the above-mentioned INP instrumentations can provide~~ We compare the different approaches to infer the impact of particle size on ice nucleation. INP measurements from different approaches allow us to understand aerosol properties. For example, we could have active INPs from pollen particles above 10 μm, which are not captured by the PM$_{10}$ measurements, but submicron biogenic macromolecules down to below 100 nm would be. With the impinger, we capture particles larger than 10 μm but no particles smaller than 500 nm. Therefore, different approaches are needed to capture both extreme ends of the size range. Similarly, WT-CRAFT collected particles smaller than 10 μm efficiently and uses smaller droplet sizes than DRINCZ for freezing experiments and thus can be assessed for ice nucleation temperatures down to -30 °C extending the temperature range of the DRINCZ approach (-22 °C) by 8 °C. The broader coverage of particle sizes ~~, types, as well as freezing temperatures~~ and temperatures measured by the combined methods allows for a better representation of ambient INPs.

Table 1. Summary of INP sampling and measurement techniques applied in the present study. For the droplet freezing techniques (i.e., DRINCZ and WT-CRAFT), the lower temperature range represents the homogeneous freezing temperature, where pure water is observed to freeze at the corresponding droplet size. In HINC, homogeneous freezing is observed at -38 °C, which is to be expected given that the droplet sizes are much smaller than the other instruments. In this work, HINC was only operated at -30 °C in the immersion freezing mode (RH$_w$ = 104 %).

Sampling site	Aerosol sampling	INP measurement	Flow rate	Aerosol size	Droplet size	Droplet #	LOD	Temperature	Time interval
Aerosol container	Impinger	DRINCZ	300 LPM	0.5∼20 µm	50 µL	96	0.0002 INP L^{-1} air	-5∼-22 °C	1 hour
Aerosol container	HINC	HINC	0.25 LPM	< 2.5 µm	2∼5 µm[*]	700/cc[**]	0.04 INP L^{-1} air	-30 °C	1/3 hour
GVB observatory	LVS + PM$_{10}$ inlet	DRINCZ	38.3 LPM	< 10 µm[***]	50 µL	96	0.0002 INP L^{-1} air	-5∼-22 °C	8 hours
GVB observatory	TSP inlet	WT-CRAFT	5.4 LPM	< 10 µm[***]	3 µL	70	0.003 INP L^{-1} air	0∼-30 °C	96 hours

[*] Depending on aerosol sizes and compositions.

[**] Assuming droplet size of 5 µm before water vapor competition.

[***] The PM$_{10}$ and WT-CRAFT samples were collected on the 0.4 and 0.2 µm polycarbonate membrane filters, respectively. The small-sized particles can be sampled by interception and diffusion, even for those below the filter pore sizes. Therefore, there is no lower size limit because the entire airflow is directed through the filter.

2.3 Heat treatments

Macromolecules originating from biological species (e.g., bacteria and phytoplankton) that typically comprise of proteins can effectively catalyze ice nucleation (Pummer et al., 2015; Hill et al., 2016). Proteins are susceptible to heat, i.e., heating effectively unfolds the proteinaceous structure, degrading the IN ability of the particles (Creamean et al., 2021; Hill et al., 2016; McCluskey et al., 2018; Pummer et al., 2015). For the heat treatment, liquid samples from the impinger and washout of PM$_{10}$ filters and TSP filters (for WT-CRAFT analysis) were subjected to 95 °C for 20 min. Subsequently, after being stabilized to room temperature, they were redistributed to PCR trays for INP analysis using DRINCZ. By comparing the IN activity after heating, it is possible to assess the contribution of heat-labile species to the INP population, which could be used as a proxy to indicate the presence of biological INPs. We note that such heat treatment could exclude lower molecular weight samples yet still imply that proteinaceous aggregates are present (Seifried et al., 2023). Thus, any effect of heat treatment on the INP concentration would be due to the contribution of heat-labile particles from biogenic sources. Post-campaign heat tests were conducted in the laboratory. To elucidate the relative change of INPs affected by degradation due to freezing storage only, we repeated the INP concentration analysis for original impinger samples that were selected for heat treatment. Heat treatment was applied to all PM$_{10}$ filter samples, and 14 impinger samples overlapping with the WT-CRAFT time window for repeated INP analysis and heat treatment for comparison.

2.4 Particle chemical composition analysis

2.4.1 CCSEM/EDX for impinger droplet residual samples

Computer-controlled scanning electron microscopy with energy-dispersive X-ray spectroscopy (CCSEM/EDX) was utilized to automatically probe the morphology and elemental composition of individual particles in a series of selected impinger samples collected on the Aluminum foils (Laskin et al., 2006). The system includes an environmental scanning electron microscope (ESEM, Quanta 3D, Thermo Fisher) equipped with an FEI Quanta digital field emission gun operated at 20 kV and 480 pA

220 with 30 μm aperture and spot size of 6.0 nm to retrieve the ESEM images, which were used to retrieve the morphologies of individual particles (Lata et al., 2021). These individual particles are recognized based on the difference of brightness and contrast between particles and substrate in ESEM images. The ESEM was also equipped with an EDX spectrometer (EDAX, Inc.) to determine the relative percentages of 12 elements (C, N, O, Na, Mg, Si, P, S, Ca, Mn, Fe, and Zn) in the individual particles (see Table D1). Applying a k-means clustering algorithm on all analyzed particles using their atomic percentages

225 (Hartigan and Wong, 1979), we categorized components inside each particle as Salt (Na + Mg $\geq$ 15 %), Si-dust (Si + Ca + Fe $\geq$ 15 % & Si $\geq$ Fe), Fe dust (Si + Ca + Fe $\geq$ 15 % & Fe > Si), Sulfate (S) (S $\geq$ 2 %), Phosphorus (P $\geq$ 1 %) and metal containing particles (Mn + Zn $\geq$ 15 %). The number of clusters was determined using the silhouette method (Kodinariya and Makwana, 2013). Then based its composition, we classified individual particle as salt containing particle, dust containing particle, metal containing particle, and P containing particle. It should be noticed that particle can be clustered into multiple

230 classes. For instance, if a particle only fulfils Na + Mg $\geq$ 15 % and Si + Ca + Fe $\geq$ 15 % & Si $\geq$ Fe, its composition is classified as (salt + Si - dust). It should be noted that the chamber was operated at 293 K under vacuum conditions (ca. 2 × 10^{-6} Torr). Thus, volatile and semi-volatile components might have been evaporated. For selected impinger samples as case studies indicated in Section 3.3.2, the total number of particles analyzed by CCSEM-EDX were 1171, 1286 and 1016 for Impinger_high, Impinger_moderate and Impinger_low samples, respectively.

235 ### 2.4.2 Single particulate matter chemical composition using Raman microspectroscopy on impinger samples

Selected samples were characterized with Raman microspectroscopy using a Thermo Scientific DXR Raman Spectrometer coupled to an Olympus BX 20 microscope and a CCD to capture images of the particle as the analysis was performed (Deng et al., 2014). The analysis was performed with a 532 nm frequency doubled Neodymium-doped Yttrium orthovanadate (Nd: YVO4) diode-pumped solid-state laser with 3 Mw power. A 50× objective (Thermo Scientific) was used to find a single

240 particle that was then sampled for bond composition following the procedures used in previous studies (Deng et al., 2014). Ten exposures at ten seconds each were averaged to smooth the sample spectrum. Samples that showed signs of fluorescence were not analyzed past identification of the fluorescence, as there was no way to tell whether additional peaks were obscured by the fluorescence signal.

Peaks were classified based on Larkin (2017) and samples were classified into broad categories. As the environmental

245 samples contain both internally and externally mixed aerosol particles, a more detailed classification was not possible. The

samples were classified as metal-containing, nitrogen-containing, sulfur-containing, organic-containing, and aromatic-ring-containing (note that particles can be placed into more than one category based on composition).

2.4.3 JEOL SEM-EDX for PM$_{10}$ filter samples

The JEOL scanning electron microscopy – energy-dispersive X-ray spectroscopy (SEM-EDX) system (Model JSM-6010LA) was used to assess the elemental composition of aerosol particles collected on the PM$_{10}$ filters. Briefly, this system allowed us to characterize the atomic percentage of 14 elements, including N, O, Na, Mg, Al, Si, P, S, Cl, K, Ca, Mn, Fe, and Zn, on a single particle basis (see Table D2). All analyses were performed under a constant measurement condition, which is a 20 keV electron beam accelerating voltage and a 10 mm distance between the SEM objective lens and the specimen surface. Because the particles were collected on polycarbonate filters, it was not possible to determine the atomic percentage of carbon. Instead, SEM-EDX data were mainly used to determine the presence or absence of mineral dust- and/or sea salt-relevant elements using the simple particle-type classification method, which was previously applied for the Alaskan Arctic aerosol characterization study Hiranuma et al. (2013).

A total of 627 aerosol particles (i.e., 6 filter samples and approximately 100 particles per sample) were analyzed in this study. Individual particles were assessed for their x-axis and y-axis segment diameters, and a cross-sectional average diameter was computed for each particle. The largest particle analyzed was 6.04 μm in diameter. It should be noted that the edge of filter pores can be misidentified as particles under CCSEM-EDX due to similar brightness and contrast as particles. The lower detection limit for the JOEL SEM method is approximately 0.5 μm particle diameter. Thus, we decided to manually analyze a subset of particles with a regular SEM-EDX system. We note that the manual operation of SEM-EDX is a time-consuming and labor-intensive process, so its application during this study was limited. For this reason, a few samples were selected to study in greater detail. A subset of single particles was selected on each filter to analyze particle composition, with at least 100 randomly selected particles (at least 25 particles per 128 μm × 96 μm cross-section) across each filter. to give an approximation of population chemical composition and major particle groups (i.e., mineral dust- or sea salt-rich particles). No specific particle size or shape was pre-selected for analysis. Instead, a range of sizes and shapes was targeted to give the best approximation of overall population chemistry.

2.5 Complementary measurements and analyses

2.5.1 Particle size distribution

The size distribution of submicron particles was measured using a scanning mobility particle sizer (SMPS, Model 3938, comprising a 3082 classifier, a 3081 long differential mobility analyzer and a 3787 CPC, TSI Inc.). The sampling flow rate of the SMPS was 0.6 L min^{-1} with a sheath-to-sample ratio of 10:1, leading to a range from approximately 15 to 600 nm in electrical mobility diameter. In addition, multiple charge correction was applied to account for the misclassification of large particles with multiple charges. Parallel to the SMPS, the size distributions of coarse-mode (ranging from approximately 0.5 to 20 μm in aerodynamic diameter) particles were analyzed by an aerodynamic particle sizer (APS, model 3321, TSI Inc.) at a flow

rate of 1 L min^{-1}. For the aim of cross-comparison, the electrical mobility diameters obtained from SMPS and aerodynamic diameters from the APS were converted to volume-equivalent diameters assuming an average particle density of 2 g cm^{-3} (Li et al., 2022; Tobo et al., 2019) and a dynamic shape factor of 1.2 (Li et al., 2022; Thomas and Charvet, 2017). A set of identical SMPS and APS was available at both GVB observatory and aerosol container for this study.

2.5.2 Particle fluorescence

The concentration of biological fluorescent particles with diameters ranging between 0.5 and 20 μm was monitored using the wideband integrated bioaerosol sensor (WIBS-5/NEO, DMT) on a single particle basis, downstream of the inlet of the aerosol container. The WIBS uses ultraviolet light to trigger the excitation of particles and to detect the emissions scattered from the fluorescent particles (Toprak and Schnaiter, 2013). The wavelengths of excitation and emission were specifically designed to probe biological fluorophores, e.g., trytophan-containing proteins, NAD(P)H and riboflavin, which are ubiquitous in the airborne microbes (Pöhlker et al., 2012). The resulting total fluorescence was then measured in three fluorescence channels: FL1 (310–400 nm) and FL2 (420–650 nm) following a 280 nm excitation, and a 370 nm excitation for channel FL3 (420–650 nm). Each individual particle is identified to be fluorescent in any channel when the intensity of its fluorescence emission is higher than the baseline threshold. However, the fluorescent signals from WIBS may misidentify non-biological particles with fluorescent signatures, such as some dust particles, HULIS and PAHs (Toprak and Schnaiter, 2013). These misclassifications could be suppressed by characterizing the fluorescence in different channels independently, which allows particles to be classified into different fluorescence categories (Savage et al., 2017; Perring et al., 2015). The new fluorescence categories are named A, B, C, AB, AC, BC and ABC based on the detection of activation in the original channels (i.e., FL1, FL2 and FL3), signifying particle fluorescence detected in channel FL1 only, FL2 only, FL3 only, FL1 and FL2, FL1 and FL3, FL2 and FL3 and all three channels, respectively. More details are given in Fig. 1 of Savage et al. (2017); Perring et al. (2015). To minimize the false-positive signal of non-biological particles that are fluorescent, the category "AC + ABC" (a particle fluoresces in both the FL1 and the FL3 channels but is not activated in the FL2 channel) was applied as a proxy for detecting biological fluorescent aerosol particles, with reduced remaining interference from non-biological sources (Toprak and Schnaiter, 2013).

2.5.3 Black carbon

Equivalent black carbon (eBC) concentration data were used to assess the potential contribution of BC on INP abundance. The eBC was measured using a particle soot absorption photometer (PSAP, Radiance Research), with which the light absorption coefficient (b_{abs}, m^{-1}) can be determined at three absorption wavelengths (Gilardoni et al., 2019). eBC concentration is derived from the light absorption coefficient at 660 nm. The mass concentration of BC (M_{BC}, g m^{-3}) can be estimated by dividing b_{abs} by the constant mass absorption cross-section of BC (MAC, m^2 g^{-1}) of 10.0 ± 0.2 m^2 g^{-1} (Sinha et al., 2017).

2.5.4 Meteorological conditions

We investigated the relationships between INP concentrations and the meteorological variables, including ambient temperature
(T_{env}), relative humidity (RH_{env}), pressure (p_{env}), wind speed (ws) and wind direction (wd). The meteorological measurements for correlating samples from the aerosol container were conducted using an automatic meteorological station (MetSystems model WS-501, OTT). For measurements at the GVB observatory, we used the meteorological data from the Amundsen-Nobile Climate Change Tower configured with a set of meteorological sensors (details described in Mazzola et al., 2016).

2.5.5 Ion chromatography

The ionic compositions of the filters collected at GVB observatory in parallel with LVS PM$_{10}$ filters were measured in aqueous extracts prepared prior to analysis using the ion chromatography following the procedures described in Becagli et al. (2011). The resulting ionic compositions involve many cations, inorganic anions (see detailed ion species in Becagli et al., 2011), methanesulfonic acid (MSA) and oxalate.

2.5.6 Backward trajectory analysis

Air mass backward trajectories were computed with the Hybrid Single-Particle Lagrangian Integrated Trajectory (HYSPLIT) model available *online* (Rolph et al., 2017; Stein et al., 2015). Ten-day (240-h) backward trajectories were computed 5 m a.g.l from the sampling location every six hours during the sampling period. To account for wet deposition, complete particle loss was assumed at 7 mm rainfall along the trajectory (Gong et al., 2020). The rainfall was summed along the trajectory and the trajectory origin is reported as either the time and location where cumulative rainfall exceeded 7 mm or the location of the air mass 240 hours before the sampling time, whichever was earlier. Air mass origin is reported in broad geographic terms, with oceans named according to commonly accepted names as defined by the U.S. Board on Geographic Names and terrestrial regions defined by continent. The Arctic regions were defined as occurring above 60 °N latitudes. Back trajectory origins were determined, accounting for particle deposition due to wet deposition.

3 Results and discussion

3.1 Overview of atmospheric INP concentration

Figure 3 (a) shows the overall N_{INP} range as a function of ice nucleation temperature (T) at Ny-Ålesund during the NASCENT campaign (Pasquier et al., 2022a) from October to November 2019. In general, measurements among different techniques agree with each other as demonstrated by the substantial overlap. Specifically, the median N_{INP} at T = -20 °C measured with the PM$_{10}$, impinger and WT-CRAFT instruments were approximately 1.0×10^{-2}, 2.7×10^{-2} and 0.7×10^{-2} L^{-1}, respectively. In addition, the variability of N_{INP} as a function of T changes with T. In particular, for the PM$_{10}$ and impinger samples, N_{INP} varied over 3 orders of magnitude at mid-range activation temperatures (T = -16 $\sim$ -14 °C), but the variation range shrunk as T increased or decreased. This could be simply attributed to the reduced number of available observations as the lower and upper
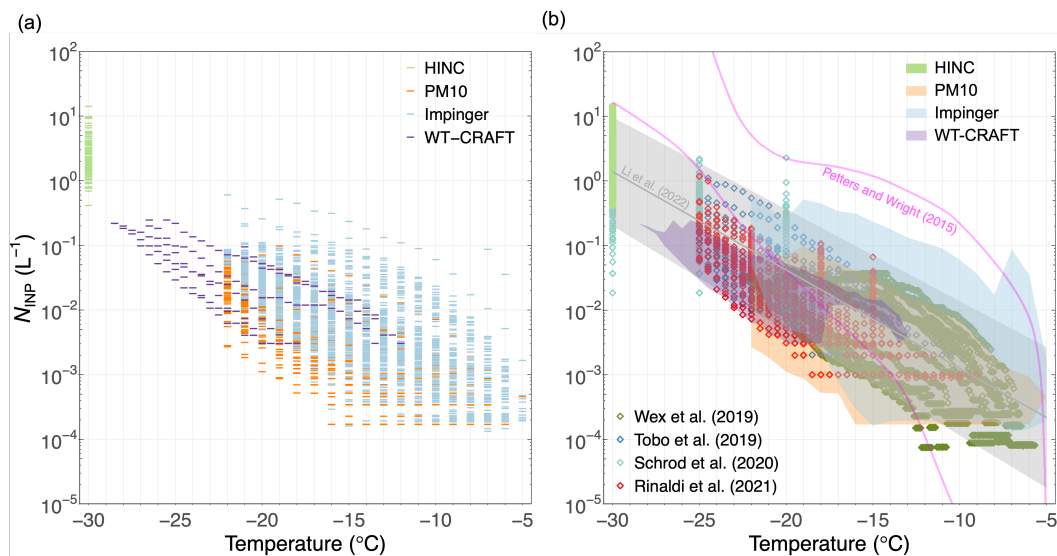
Figure 3. Ambient INP concentration as a function of ~~activation~~ temperature for (a) observations of N_{INP} (symbolized with "-") including the sampling and measurements with HINC (T = -30 °C) and the impinger (-22 °C ∼ -5 °C) at the aerosol container, and with the PM$_{10}$ filter (-22 °C ∼ -5 °C) and WT-CRAFT (-30 °C ∼ -12 °C) at GVB observatory during autumn 2019 in Ny-Ålesund. (b) comparison of our observations to literature data. The area between two lines in magenta is a compilation of INP concentrations determined from precipitation samples from the mid-latitude (Petters and Wright, 2015). The light gray line (median) and the shaded area (95 % confidence interval) denote the INP parameterization developed from the Ny-Ålesund data during the NASCENT campaign in autumn 2019 and spring 2020 (Li et al., 2022). INP concentration data from Rinaldi et al., 2021 (spring and summer), Schrod et al., 2020 (year-long), Tobo et al., 2019 (spring and summer) and Wex et al., 2019 (spring, summer and autumn) measured at the same location are also presented in colored diamonds.

instrument detection limits are approached (see Section 2.2.1). In addition, the distribution of WT-CRAFT INP data overlaps largely with PM$_{10}$ and impinger data, which is to be expected since they were both taken at the GVB station. Additionally, the

340 INP data for WT-CRAFT and PM$_{10}$ are approximately log-linearly extrapolatable, although some variation is observed due to the limited sample number and coarse temporal resolution.

Compared to the global range of N_{INP} derived from precipitation samples collected in the continental mid-latitudes (Petters and Wright, 2015) (3 ~~b~~b), the average N_{INP} observed in the Arctic is approximately 2 orders of magnitude lower. However, at the highest T (-5 to -7 °C), N_{INP} observed with the impinger were close to or higher than the global average level (Petters

345 and Wright, 2015), despite high uncertainties may arise. This indicates a potentially significant contribution of biological INPs in the Arctic. The Arctic INP parameterization (Li et al., 2022) derived from the same campaign developed from impinger and HINC data from both autumn 2019 and spring 2020 generally agreed with the observations from PM$_{10}$ and WT-CRAFT. Moreover, Figure 3 (b) also displays a compilation of N_{INP} measurements from recent ground-based observations in Ny-Ålesund for comparison. Note that besides the natural variability of N_{INP}, a number of factors (e.g., systematic error of each

350 instrument, sampling volume and seasonality) could contribute to the differences in observed N_{INP} among studies. Nevertheless,
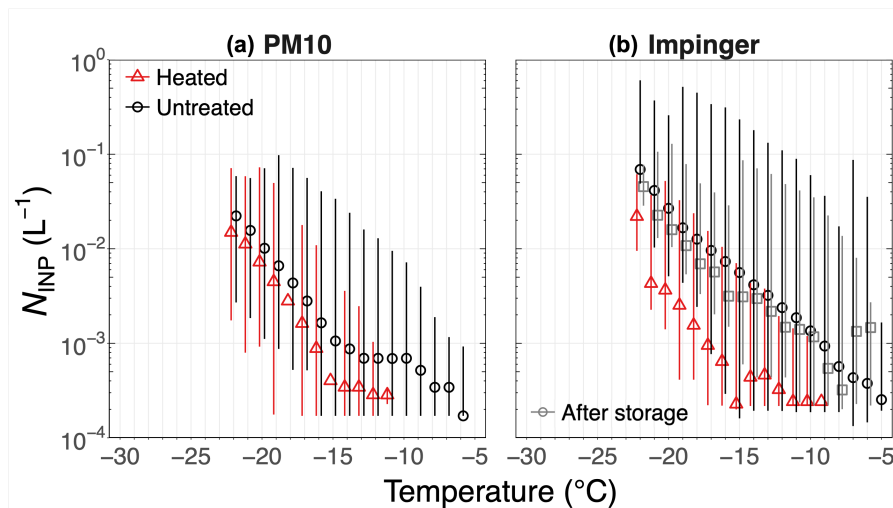
Figure 4. Ambient INP concentration with and without heat treatment conditions as a function of ~~ice activation~~ temperature for different samples: (a) PM$_{10}$ ~~,~~and (b) impinger~~and (c) WT_CRAFT)~~. The ~~hollow circles shown in (a) and (b)~~ symbols represent the median N_{INP} of all samples collected during October-November 2019, and the vertical ~~extensions~~ lines represent the 5 - 95 % percentile of the measurements. ~~For~~ The heat treatment was not conducted onsite for impinger samples shown in (b)~~, the heat treatment was not conducted onsite~~. Instead, the frozen samples were reanalyzed (gray ~~open circles~~squares) after storage in the laboratory and then subjected to heat treatment.~~The open circles shown in (c) denote the 7 individual INP spectra during the autumn 2019 campaign in Ny-Ålesund (from 12: 43 UTC 03/10/2019 to 12:49 UTC 30/10/2019 at an approximately 4-day sampling interval). The filled circles in (c) represent the sample taken from 10:37 UTC 19/10/2019 to 12:15 UTC 23/10/2019 for original INP analysis and reanalysis after heating.~~

the majority of literature N_{INP} overlapped with our observation range, except Schrod et al. (2020) who observed systematically higher N_{INP} at T = -20 °C, and data from Wex et al. (2019) at higher T who measured lower INP concentrations, likely due to different ~~sensitivities~~ detection threshold of the instruments (i.e., LOD) and the seasons during which they took measurements because a different season could imply different sources and abundance of INPs.

355   To detect the presence of proteinaceous biological ice-nucleating entities, heat treatment was applied to sample solutions. Figure 4 compares the overall INP spectra ~~between different untreatedand heated samplesusing different sampling and INP instruments. The range of activation temperatures measured is different for WT-CRAFT and PM$_{10}$ and impinger samples, likely due to the different instrumentation limits (i.e., droplet volume).~~ of untreated, stored, and heat-treated samples. For untreated samples, the overall INP concentrations at the same ~~activation~~ temperatures sampled by the impinger from the aerosol container

360   were systematically higher (ca. 2 to 3 times) ~~compared to~~ than those sampled by PM$_{10}$ filters at the GVB observatory. ~~At the GVB observatory,~~ The differences in N_{INP} ~~sampled with the TSP inlet for WT-CRAFT analysis were comparable to those measured from PM$_{10}$ filters in the overlapping temperature range. Despite the longer sampling duration (> 3 days), this study includes the WT-CRAFT N_{INP} data as it compensates the immersion freezing data lower than the temperature range measured by DRINCZ and bridges the gap towards HINC measurements. The differences in N_{INP} between the impinger samples which~~

15

365 between the impinger and PM$_{10}$ filter samples could be due to the storage and analyzing procedure. The impinger samples were analyzed for N_{INP} directly after ~~the collection on site~~ collection on-site, and the PM$_{10}$ filters ~~which we believe is due to the frozen storage~~ were stored frozen at -20 °C and analyzed ~~for N_{INP}~~ 1.5 years after the campaign in the laboratory. Beall et al. (2020) revealed that heat-labile INPs tend to be more sensitive to storage, i.e., storage and re-thawing of heat-sensitive samples in the case for our PM$_{10}$ samples (Figure 4 ~~a~~a), which could conceivably degrade the IN activity ~~(although the extent~~

370 ~~is unknown). This hypothesis also held true~~. The number of small organic INPs could be reduced due to aggregation when enriched solute becomes incorporated into the ice phase during storage. Additionally, as the solution phase is enriched during freezing, smaller INPs may be absorbed onto the surface of larger particles, thus resulting in the coalescence of the INPs (Beall et al., 2020). However, a clear mechanism for the INP losses after cryo-storage is not reported since they lack the identities of observed INPs. Similarly, a slight reduction in median INP concentrations was also observed for impinger samples

375 ~~(see Fig. 4 b) when~~ at most of the investigated temperatures when they were stored and reanalyzed in the laboratory (~~"after storage" in gray). Here overall~~ see "after storage" in gray symbols in Fig. 4 b). The above reasons, however, would not explain degradation in the PM$_{10}$ samples; as such, we believe that the lower N_{INP} ~~decreased nearly at all investigated temperatures. Additionally, with different sampling flow rates and time, the total~~ in the PM$_{10}$ samples is indicative of a size dependency since the impinger samples include particles larger than 10 μm which are excluded in the PM$_{10}$ samples. This conclusion is also

380 supported by the N_{INP} from impinger being systematically higher than those from the PM$_{10}$ samples (see Fig. 3). The N_{INP} of the impinger samples before and after storage largely overlap in freezing temperatures. On conducting a t-test, this difference was insignificant at most investigated temperatures (not shown). Given the similar volume of air collected ~~by each impinger, PM$_{10}$ and WT-CRAFT filter sample was~~ in each sample (approximately 18 m^3, 18.4 m^3 ~~and 20.2 m^3, respectively. Given the similar volume of air collected in each sample, another~~ for impinger and PM$_{10}$ filter sample, respectively), a possible reason for

385 the differences in INP population was due to different size thresholds (as alluded above) based on the sampling efficiency (i.e., impinger: >0.5 to 20 μm ~~, and~~ PM$_{10}$ filters: < 10 μm~~, TSP inlet for WT-CRAFT: > 0.2 m~~) at which the aerosols were collected using the ~~three~~ two sampling techniques. ~~In particular, aerosol samples collected by the impinger included particles~~ Particles larger than 10 μm ~~, which are frequently~~ collected by the impinger are effective INPs given their large sizes (DeMott et al., 2015; Mason et al., 2016) despite their relative scarcity in the ambient air. In terms of heat sensitivity, the general degradation

390 of N_{INP} for all samples after being heated at 95 °C for 20 minutes, particularly at $T \geq$ -15 °C, suggests that heat-labile IN active proteins or biological macromolecules likely contribute to INP sources in the Arctic during our measurement season. The remaining IN active materials could be mineral dust or heat-resistant organics (Conen et al., 2016; Hill et al., 2016), for which N_{INP} were similar for PM$_{10}$ and impinger samples. ~~Specifically, one interesting exception highlighted in Fig. 4 (c) (filled circles) displayed both high N_{INP} and heat-insensitivity for the sample collected from 19/10 to 23/10 in 2019. More evidence~~

395 ~~will be~~ More evidence is provided by measurements with finer ~~resolutions~~ resolution to unveil the INP abundance and potential sources (see Section 3.3).

3.2 N_{INP} correlations with meteorological and aerosol physicochemical variables

Table 2 summarizes the Pearson correlation coefficients (r) between the entire time series of N_{INP} and several physicochemical and meteorological variables. It can be seen that for most cases, $-0.5 < \rho < 0.5$, suggesting no strong correlation in general. The absence of a strong correlation demonstrates that during the 6-week measurement campaign, a mixture of parameters correlated with the observed INP population. However, the actual level of correlations could be underestimated for all cases, because in order to synchronize N_{INP} and other measured parameters with different time resolutions, the variability could be concealed when averaging the variable over a period of time, e.g., averaging 3-min particle size distribution data for comparison with N_{INP} over several hours in a high-volume filter sample. In addition, the level of statistical significance was reduced due to the shrunk data sets. The aforementioned rationale supports the need for high time resolution of N_{INP} measurements.

~~Pearson correlation coefficients (r) between INP concentration at different nucleation temperatures (sampled by impinger -6 ~ -18 °C and HINC -30 °C at the aerosol container, separated by the double solid lines in the upper part of the table) to aerosol physicochemical and meteorological variables: aerosol concentration of particles within different diameter ranges ($n_{0.01\sim0.1}$, $n_{0.1\sim0.5}$, $n_{>0.5}$, $n_{0.5\sim1}$, $n_{1\sim2.5}$ and $n_{>2.5}$, with diameters in m), aerosol surface area concentration of particles with diameter at different size ranges ($S_{>0.5}$ and $S_{<2.5}$, with size unit in m), equivalent black carbon concentration (eBC), fluorescent particle concentration defined by different categories (n_{fluor}, n_{FL1}, n_{FL2}, n_{FL3} and $n_{\text{AC+ABC}}$, according to the criteria of classification defined in Section 2.5.2) and meteorological variables (ambient temperature T_{env}, RH RH_{env}, pressure p_{env}, wind speed ws and direction wd). Note that different aerosol size-resolved variables were correlated with N_{INP} at different nucleation temperatures due to different size cut-offs of INP sampling/measurement, impinger sampled N_{INP} at T = -6, -9, -12, -15, -18 °C with a lower size threshold of 0.5 m, and HINC measured N_{INP} at T = -30 °C with an upper size limit of 2.5 m, located in the aerosol container. Correlations between N_{INP} (-6 ~ -18 °C) and sodium, ammonium, calcium, nitrate, sulfate and methanesulfonic acid (MSA) were derived from the filter samples collected at GVB in parallel with PM$_{10}$ INP filters using the ion chromatography analyses (separated by the double solid lines in the lower part of the table).~~

Regarding the correlations between N_{INP} and size-resolved aerosol concentrations, it should be noted that increasingly higher correlations of N_{INP} were found with aerosol concentrations with increasingly larger size ranges at most nucleation temperatures, revealing the fact of the increasing contribution of larger-sized particles to INP populations. Nevertheless, the overall absence of strong correlations is presented, which is in agreement with some previous studies (e.g., Li et al., 2022; Paramonov et al., 2020; Lacher et al., 2018). The absence of a notable correlation was also observed between N_{INP} and supermicron aerosol particles, despite previous findings (e.g., DeMott et al., 2015; Mason et al., 2016) suggesting ~~them to constitute the major fraction of the observed INP population~~ a positive correlation between the concentration of INPs and supermicron aerosols. One important reason is that INPs are only a small subgroup of ambient aerosol particles. ~~As the~~ The time series of the activated fraction of INPs shown in Fig. 5 ~~, during the entire campaign,~~ implies that approximately 1 out of 10^5 ambient aerosol particles on average acted as INPs at ~~an activation temperature of~~ -15 °C. Therefore, a minor fluctuation of IN inactive components in the total aerosol populations, e.g., via a sudden increase of coarse-mode sea salt, would mask the correlations. Additionally, the long-range transport of INPs from mid- and high-latitudes in the upper troposphere, which

is considered to be another important source of INPs in the remote Arctic (e.g., Porter et al., 2022; Schmale et al., 2021; Wex et al., 2019), may alter the population of INPs towards smaller sizes due to the size-dependent deposition processes during atmospheric transport (Lacher et al., 2018). Similarly, strong correlations between N_{INP} and available surface area concentrations (i.e., $S_{>0.5}$ and $S_{<2.5}$ for correlating N_{INP} sampled by impinger and HINC, respectively) were not found.

435 Strikingly, the correlations between N_{INP} and fluorescent particle number concentrations, which have been used as a proxy for identifying bioaerosol (e.g., Toprak and Schnaiter, 2013; Savage et al., 2017) were relatively strong with statistical significance compared to other observed variables. This observation was particularly true towards warm nucleation temperatures, consistent with our inference from our heat test results shown in Section 3.1. It is therefore reasonable to conclude that when the surface was free from snow and ice (as it was during most of the time during our measured period in the high Arctic), highly IN-active

440 bioaerosols originating from the terrestrial and marine environments could act as dominant local INP sources. Additionally concerning eBC, the overall weak to no correlations with N_{INP} at all investigated temperatures suggest negligible contributions from eBC, which is in agreement with the findings that BC is not an effective INP in the immersion freezing mode in the MPC temperature regime (-38 °C $< T <$ 0 °C), both from field (Paramonov et al., 2020; Lacher et al., 2018; Kupiszewski et al., 2016) and from laboratory studies (Kanji et al., 2020; Mahrt et al., 2018; Chou et al., 2013; Friedman et al., 2011).

Table 2. Pearson correlation coefficients (r) between INP concentration at different nucleation temperatures (sampled by impinger [-6 ∼ -18 °C] and HINC [-30 °C] at the aerosol container, the upper part separated by the double solid lines in the upper part of the table) to aerosol physicochemical and meteorological variables: aerosol concentration of particles within different diameter ranges ($n_{0.01\sim0.1}$, $n_{0.1\sim0.5}$, $n_{>0.5}$, $n_{0.5\sim1}$, $n_{1\sim2.5}$ and $n_{>2.5}$, with diameters in μm), aerosol surface area concentration of particles with diameter at different size ranges ($S_{>0.5}$ and $S_{<2.5}$, with size unit in μm), equivalent black carbon concentration (eBC), fluorescent particle concentration defined by different categories (n_{fluor}, n_{FL1}, n_{FL2}, n_{FL3} and n_{AC+ABC}, according to the criteria of classification defined in Section 2.5.2) and meteorological variables (ambient temperature [T_{env}], RH [RH_{env}], pressure [p_{env}], wind speed [ws] and direction [wd]). Note that different aerosol size-resolved variables were correlated with N_{INP} at different nucleation temperatures due to different size cut-offs of INP sampling/measurement, impinger sampled N_{INP} at T = -6, -9, -12, -15, -18 °C with a lower size threshold of 0.5 μm, and HINC measured N_{INP} at T = -30 °C with an upper size limit of 2.5 μm, located in the aerosol container. Correlations between N_{INP} (-6 ∼ -18 °C) and sodium, ammonium, calcium, nitrate, sulfate and methanesulfonic acid (MSA) were derived from the filter samples collected at GVB in parallel with PM_{10} INP filters using the ion chromatography analyses (below the double solid lines).

Variable	N_{INP} (T=-6°C)	N_{INP} (T=-9°C)	N_{INP} (T=-12°C)	N_{INP} (T=-15°C)	N_{INP} (T=-18°C)	N_{INP} (T=-30°C)
$n_{0.01\sim0.1}$ (L^{-1})	-	-	-	-	-	0.10
$n_{0.1\sim0.5}$ (L^{-1})	-	-	-	-	-	0.01
$n_{>0.5}$ (L^{-1})	0.24	**0.23**	0.14	0.15	0.09	-
$n_{0.5\sim1}$ (L^{-1})	0.24	**0.21**	0.13	0.13	0.07	0.17
$n_{1\sim2.5}$ (L^{-1})	0.20	**0.24**	0.15	**0.17**	0.10	**0.18**
$n_{>2.5}$ (L^{-1})	0.26	**0.31***	**0.27**	**0.28**	**0.22**	-
n_{tot} (L^{-1})	0.08	-0.04	0.00	-0.01	0.11	0.06
$S_{>0.5}$ (m^{2} L^{-1})	0.25	**0.28**	**0.20**	**0.22**	0.14	-
$S_{<2.5}$ (m^{2} L^{-1})	-	-	-	-	-	0.13
eBC (ng m^{-3})	**0.09**	-0.07	-0.04	-0.05	-0.03	0.12
n_{fluor} (L^{-1})	**0.55****	**0.36***	**0.34***	**0.38***	**0.35***	**0.20**
n_{FL1} (L^{-1})	**0.55****	**0.23**	**0.28**	**0.31***	**0.28**	**0.18**
n_{FL2} (L^{-1})	**0.56****	**0.29**	**0.27**	**0.29**	**0.27**	0.17
n_{FL3} (L^{-1})	**0.48***	**0.40***	**0.36***	**0.39***	**0.37***	0.17
n_{AC+ABC} (L^{-1})	**0.63****	**0.29**	**0.32***	**0.31***	**0.20**	0.14
T_{env} (°C)	-0.19	-0.02	0.00	0.06	0.03	**0.18**
RH_{env} (%)	-0.12	0.19	0.16	**0.21**	0.10	0.12
p_{env} (hPa)	0.00	-0.13	-0.19	**-0.24**	**-0.29**	-0.11
ws (m s^{-1})	**0.47***	**0.52****	**0.49***	**0.52****	**0.42***	0.17
wd (°)	**0.30***	**0.33***	**0.24**	**0.20**	**0.22**	0.07
Sodium (ng m^{-3})	N.A.	-0.12	-0.15	0.00	0.04	-
Ammonium (ng m^{-3})	N.A.	-0.49*	-0.08	-0.16	0.14	-
Calcium (ng m^{-3})	N.A.	0.01	0.14	0.15	0.26	-
Nitrate (ng m^{-3})	N.A.	-0.21	-0.04	-0.05	0.15	-
Sulphate (ng m^{-3})	N.A.	-0.39*	-0.12	-0.15	0.13	-
MSA (ng m^{-3})	N.A.	0.33*	0.58**	0.36*	0.43*	-

[1] r in bold text represents results with statistical significance ($p < 0.05$); r with * denote moderate correlation ($0.3 < |r| < 0.5$), and with ** indicate strong correlation ($|r| > 0.5$).

[2] "N.A." indicates that r cannot be calculated due to the limited data pairs. "-" signifies the coupled variables, i.e., N_{INP} at measured temperature and variables shown in the first column in Table 2 should not be correlated with each other due to the violation of e.g., measurement locations, size cut-off ranges between instruments.

Aside from the characterization of physical aerosol properties, we also investigated the relationships of meteorological variables with N_{INP}. Schneider et al. (2021) improved the predictability of N_{INP} by using ambient temperature as a proxy for seasonal variations of INP abundance. However, a correlation between N_{INP} and ambient temperature (T_{env}) was not observed in this work. Similarly, ambient relative humidity (RH_{env}) and pressure (p_{env}) were not (or weakly) correlated with N_{INP}. In contrast, moderate to strong correlations were found between N_{INP} ($T > -30\ °C$) and ground-level wind speed (ws), suggesting transport and advection of INPs within the sampling period. The concentration of SSA depends strongly on wind-induced wave breaking and bubble bursting (Lewis et al., 2004; Moallemi et al., 2021), which could enhance the local INP sources via, e.g., increased re-suspension of blowing dust and/or boosted SSA. Weak to moderate correlations were observed between N_{INP} and ground-level wind direction (wd), suggesting that abrupt increases of local emissions from certain directions did not contribute to specific INP sources over a relatively long time span. Particularly, the highest N_{INP} was approximately associated with the wind direction from the northern side, where there was an ice-free ocean during the entire measurement season, indicating the local marine SSA contributed to the INP concentrations. Given that sea salt is not an active INP in immersion mode, it is reasonable to conclude that the organic or biogenic components of SSA attribute to N_{INP} as supported by the heat treatment results and high correlations with fluorescent particle number concentrations.
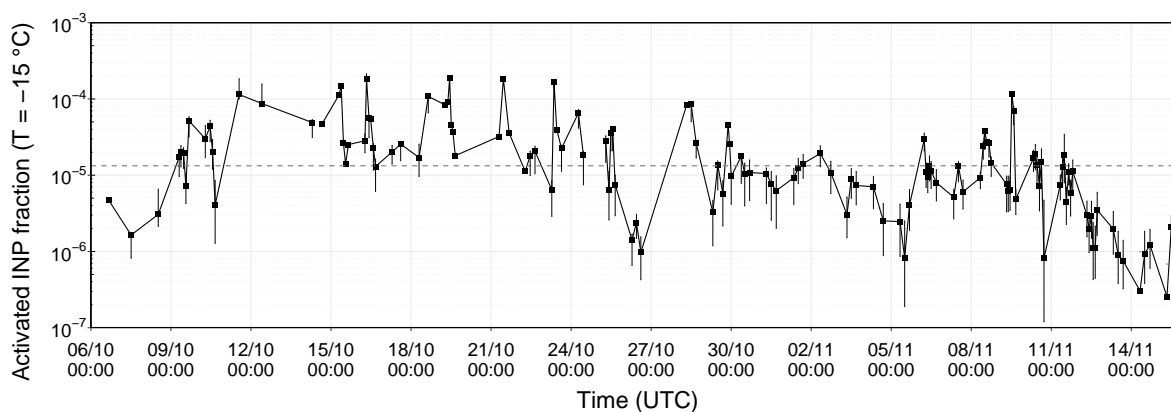
Figure 5. Time series for activated INP fraction at $T = -15\ °C$ during the autumn 2019 campaign in Ny-Ålesund. The activated INP fraction is the ratio between N_{INP} measured from impinger samples and $n_{>0.5}$ measured from the APS. Vertical extensions represent the uncertainty range within 95 % confidence intervals. The dashed horizontal line indicates the median activated fraction over the entire campaign.

The lower part in Table 2 shows the correlations between N_{INP} derived from PM_{10} filter samples and their ionic composition. Due to the limitation that the ion chromatography samples had a time resolution of two days, the number of samples was insufficient compared to other online measurement variables, resulting in the inadequate significance of correlations to N_{INP}. Nevertheless, moderate to strong correlations between N_{INP} and the concentration of methanesulfonic acid (MSA) were observed for most measured temperatures. MSA is oxidized from dimethyl sulfide (DMS), originating from emissions by oceanic phytoplankton. Despite MSA itself does not act as INP, it is a unique indicator for tracing marine biological productivity since MSA has no other natural sources (Becagli et al., 2019). Therefore, the presented correlations demonstrate an association

between INP abundance and local marine biological activity during our measured period. No correlations were manifested between N_{INP} and other trace ions, including sodium, ammonium, calcium, nitrate and sulfate.
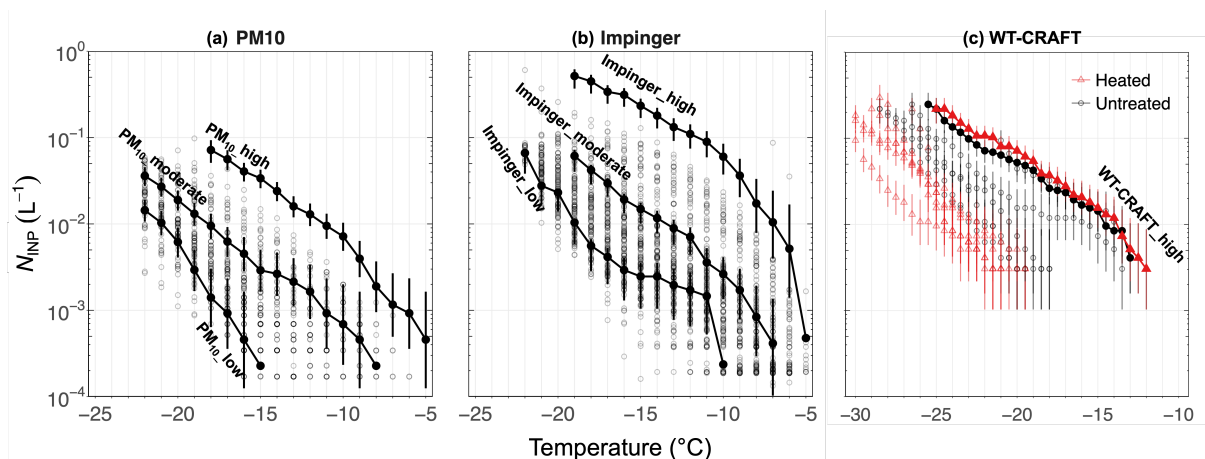
3.3 Special case studies

Figure 6. ~~Time series~~ A selection of typical INP spectra (highlighted lines and filled circles) labeled with high, moderate and low N_{INP} for ~~activated~~ case studies for (a) PM$_{10}$ filter sampling (8-h interval) from 00:00 UTC 19/10/2019, 16:00 UTC 19/10/2019 and 00:00 UTC 23/10/2019, respectively; and for (b) impinger samples sampling (1-h interval) from 11:05 UTC 21/10/2019, 06:34 UTC 24/10/2019 and 15:40 UTC 25/10/2019, respectively. (c) Individual INP ~~fraction at $T = -15\ °C$~~ spectra measured by WT-CRAFT (approximately 4-day interval) during ~~autumn~~ the 2019 NASCENT campaign from 12:43 UTC 03/10/2019 to 12:49 UTC 30/10/2019. The filled symbols with highlighted lines indicate the high-INP case measured between 12:37 UTC 19/10/2019 to 14:05 UTC 23/10/2019, overlapping the cases selected in ~~Ny-Ålesund~~ (a) and (b). The ~~activated INP fraction is~~ hollow symbols in the ~~ratio between N_{INP} measured~~ background represent all measurements from ~~impinger samples and $n_{s0.5}$ measured from~~ the ~~APS~~ corresponding offline techniques during the 2019 NASCENT field measurement. ~~Vertical~~ The vertical extensions represent the ~~uncertainty range within~~ 95 % confidence intervals ~~. The dashed horizontal line indicates~~ of the ~~median activated fraction over the entire campaign~~ experiments (only shown for selected cases in a and b for a clear display).

3.4 ~~Special case studies~~

470 ~~We further~~ To further explore the INP characteristics and sources, we focused on short-term cases ~~,~~ characterized by a broad range of N_{INP}, aerosol physicochemical properties, meteorological conditions and air mass origins. ~~Figure 6 highlights~~ Figures 6 (a) and (b) highlight the selected cases from ~~INP samples~~ all INP measurements representative of high, moderate and low INP ~~concentrations during the period of highlighted heat-resistant high-~~ number concentrations for PM$_{10}$ and impinger samples, respectively. Figure 6 (c) shows the INP measurements with WT-CRAFT and the effect of heating. The range of temperatures

475 differs between N_{INP} ~~sample shown in Fig. 4~~ measured by WT-CRAFT and DINRCZ (i.e., PM$_{10}$ and impinger samples) due to the smaller droplet volume in WT-CRAFT (see Table 1). At the GVB observatory, N_{INP} measured by WT-CRAFT was

comparable to that measured from PM$_{10}$ filters in the overlapping temperature range from -15 to -20 °C. The N_{INP} from the impinger measurements is higher than that measured from the WT-CRAFT. This could be either due to the different locations of the samples or the larger drop sizes in DRINCZ. The total volume of air sampled for the two samples is similar. The more likely explanation is that the particle size range measured by the impinger is much larger. As such, the sampled aerosol size ranges should be considered when evaluating such comparisons. Despite the longer sampling duration (> 3 days) of the WT-CRAFT N_{INP} data, we compare it to the immersion freezing data from DRINCZ because it bridges the temperature gap towards HINC measurements. Particularly, one interesting exception highlighted in Fig. 6 (c) . A broader (filled symbols labeled as WT-CRAFT_high) displayed both high N_{INP} and heat-resistant INPs for the sample collected from 19/10/2019 to 23/10/2019. To understand the properties of the heat-resistant and high N_{INP} sample in more detail with regard to aerosol properties (e.g., particle sizes), time windows that overlap with the WT-CRAFT_high case that also show a large range of N_{INP} were observed in impinger and PM$_{10}$ samples with selected for further investigation (Figures 6 a and b). With a finer temporal resolution of 1 hour and 8 hours for the selected impinger and PM$_{10}$ samples, respectively, revealing that the peak cases could explain the the INP abundance in the corresponding 4-day WT-CRAFTsample high sample could be explained by the highest concentrations. More evidence will be provided in the following subsections to elaborate on INP and aerosol features.

A selection of typical INP spectra (highlighted lines) labeled with high, moderate and low N_{INP} for case studies for (a) PM$_{10}$ filter sampling from 19/10 00:00, 21/10 16:00 and 23/10 00:00, respectively; and for (b) impinger samples sampling from 21/10 11:05, 24/10 06:34 and 25/10 15:40, respectively. The dots in the background represent all measurements from offline techniques during the 6-week field measurement.

3.3.1 Time series

Figure 7 shows the time series during the period of selected impinger samples for parallel comparison. All samples exhibited relative heat sensitivity, i.e., a reduction of INP concentrations was observed at T = -15 °C (Fig. 7 aFigure 7 a) for all selected cases (not detectable for some samples with values below the detection limit of DRINCZ). In addition, a high fluorescent particle population in the impinger_high case, (Fig. 7 bb) indicates the probable existence of biological particles, which could serve as INPs at the investigated temperatures. However, for the impinger_low case, we still observed moderate levels of fluorescent particle concentrations, possibly due to the inclusion of the non-IN-active biological or abiotic fluorescent particles. Wind conditions can impact the local aerosolization process as shown in Fig. 7 (c). The time window for the impinger_high case was dominated by northerly winds coming from the direction of the ocean (see Figs. 1 b and 7 cb and 7 c), associated with higher wind speeds compared to the moderate and low INP cases. INP enrichment in the impinger_high sample could be attributed to promoted local SSA that were IN active, likely originating from biological production and aerosolization of the marine biota (Inoue et al., 2021). The size-resolved time series in Fig. 7 (d) coincided with the INP fluctuations, i.e., a rising N_{INP} tendency with increasing coarse-mode particle number concentrations ($n_{>0.5}$) and total surface area concentrations (S_{tot}). This finding was consistent with previous ground-based observations that coarse-mode particles can strongly correlate with ambient INP population (e.g., DeMott et al., 2015, Mason et al., 2016). Concerning the moderate INP case, an abrupt rise in fine particle concentrations was observed, which had small contributions to the total surface area concentration and thus INP

abundance. The low INP case was an exception regarding $n_{>0.5}$ and S_{tot}, which exhibited moderate levels of $n_{>0.5}$ and S_{tot} but had the lowest N_{INP} among the investigated cases.
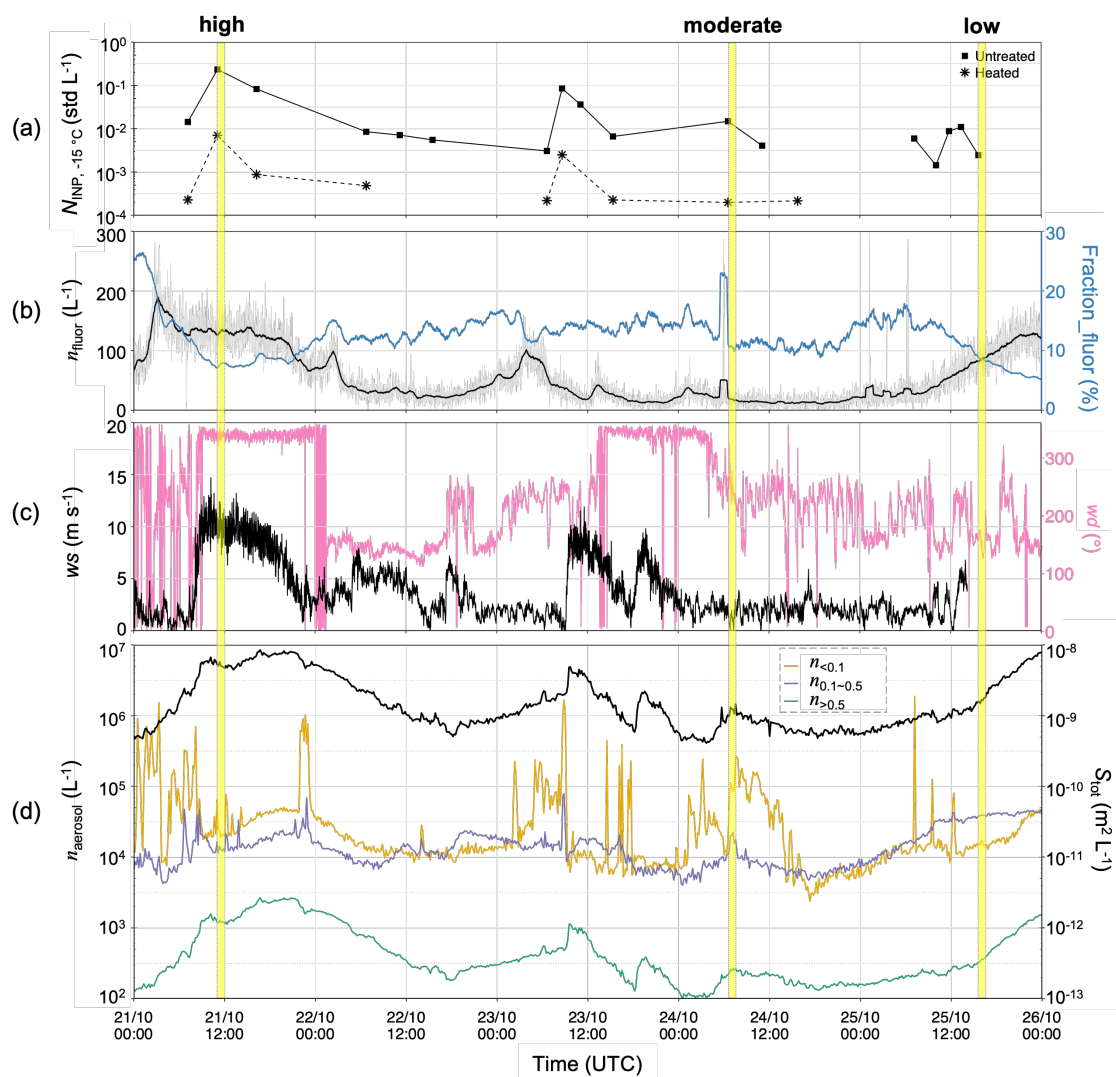

Figure 7. Time series in October 2019 during the window of selected impinger sample cases for (a) N_{INP} at $T = -15$ °C (the entire temperature spectra can be found in Fig. 6 (b)), (b) fluorescent particle number concentrations (n_{fluor}, original 1-min data in light gray, and 30-min average in black) and fractions (Fraction_fluor), (c) wind speed (ws) and direction (wd) and (d) aerosol number concentration ($n_{aerosol}$) with different size ranges and total surface area concentration (S_{tot}) calculated for relevant sizes for impinger samples.

Interestingly, we noticed similar N_{INP} - wind pattern for selected PM$_{10}$ samples (Fig. Figure 8) from GVB that high and moderate N_{INP} tended to be associated with high-speed winds with maritime origin. However, the size-resolved particle number and surface area concentrations were not good predictors for N_{INP}. The selected high, moderate and low PM$_{10}$ samples showed

515

23

comparable $n_{>0.5}$ and S_{tot} values (See Appendix B for the full range of particle size distribution). The possible reason is that aerosols sampled at the GVB observatory experienced more dilution and mixing due to the increased distance from the ocean. Additionally, as discussed in Section 3.2, the coarse time resolution of PM_{10} samples could mask the instantaneous enhanced INP loading by averaging it out over the 8-hour sampling period. Nevertheless, the high loading of particles with sizes larger than approximately 2.5 μm could contribute to the high INP case of the PM_{10} sample (shown in Fig. B1).
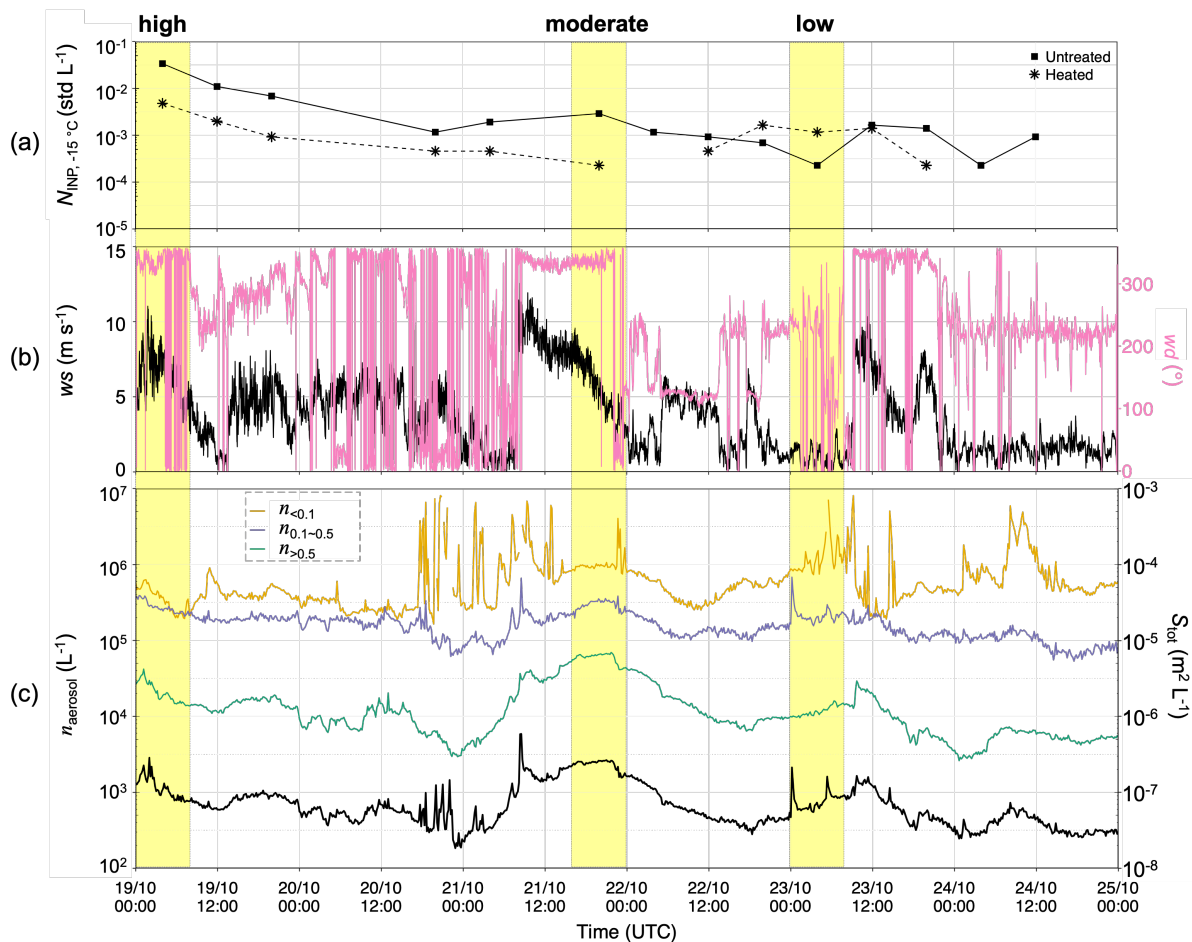
Figure 8. Time series in October 2019 during the window of selected PM_{10} sample cases for (a) N_{INP} at $T = -15$ °C (the entire temperature spectra can be found in Fig. 6 (a)), (b) wind speed (ws) and direction (wd) and (d) aerosol number concentration ($n_{aerosol}$) with different size ranges and total surface area concentration (S_{tot}) calculated for relevant sizes for PM_{10} samples.

3.3.2 Physicochemical characterization of selected samples

Similar to Fig. 4, Figure 9 displays individual INP spectra exposed to heat treatment or storage conditions for selected impinger and PM_{10} cases overlapping the period of the highlighted WT-CRAFT sample shown in Fig. 4 (c). Most selected samples were

24
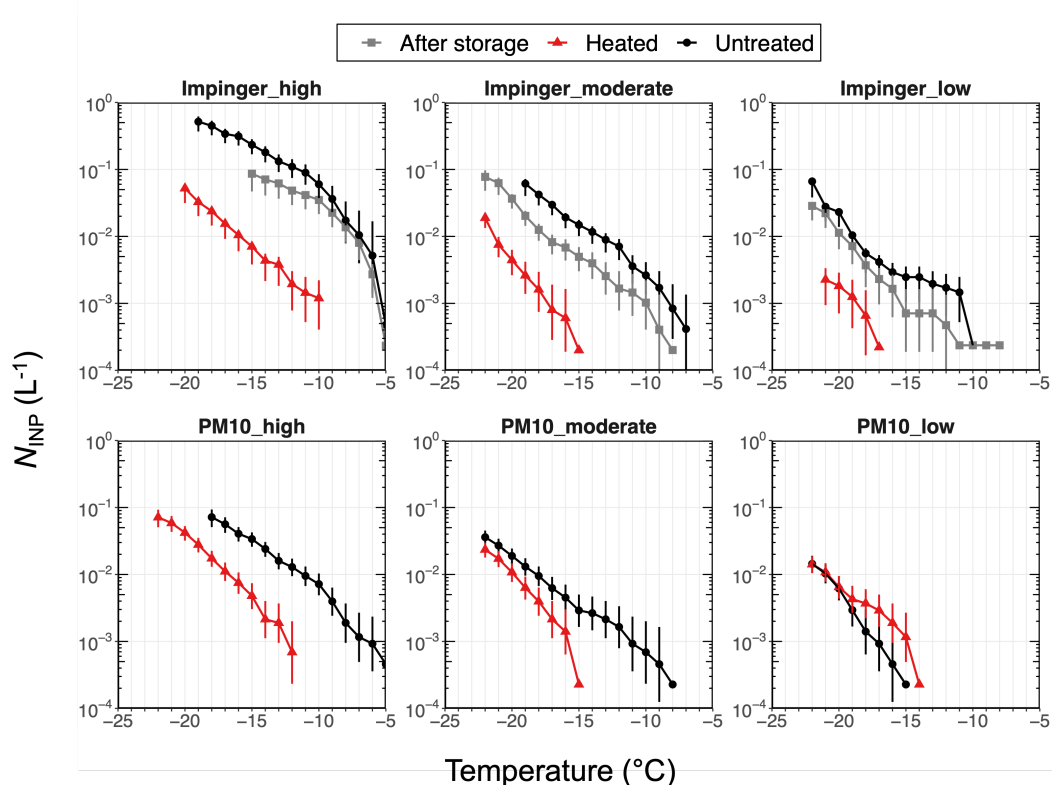
Figure 9. Selected INP spectra for untreated, heated, and storage conditions labeled high, moderate, and low N_{INP} for case studies for impinger and PM$_{10}$ samples. The vertical extensions represent the 95 % confidence intervals of the experiments. Note that the time stamps for the same N_{INP} labels regarding the impinger and PM$_{10}$ samples are different. High INP cases: 11:05-12:05 UTC 21/10/2019 and 00:00-08:00 UTC 19/10/2019, moderate INP cases: 06:34-07:34 UTC 24/10/2019 and 16:00-24:00 UTC 21/10/2019, and low INP cases: 15:40-16:40 UTC 25/10/2019 and 00:00-08:00 UTC 23/10/2019 for impinger and PM$_{10}$ samples, respectively.

heat-labile in terms of N_{INP}, especially for the impinger_high sample at temperatures higher than -10 °C, revealing potential
525 biogenic INP sources. PM$_{10}$_low was an exception, showing heat-resistant ~~aerosol compositions~~INP composition, consistent
with the heating results of the corresponding WT-CRAFT sample ~~. A likely reason could be that with a much coarser resolution
of the~~ from the GVB station (filled circles in Fig. 4c), where the 4-day ~~interval for the~~WT-CRAFT ~~sample, the~~sample possessed
relatively high N_{INP} with heat-resistance. On the other hand, the parallel PM$_{10}$ cases with much finer time resolution (i.e., 8-h
PM10_high, PM10_moderate and PM10_low samples) covered a wide range (i.e., over 2 orders of magnitude) of N_{INP} with
530 different sensitivities to heat treatment (see the second row in Fig. 9). Since N_{INP} is determined by the most active INPs in
the droplet, samples that contain heat-labile INPs ~~were overshadowed by the~~and heat-resistant INPs ~~, therefore showing no
degradation in N_{INP} (Figure 4 c). This motivates the necessity of~~ could still freeze effectively even after heating, thus masking
the effect of heating (Alsante et al., 2023). Sampling with higher temporal resolution reduces the probability of including INPs

of different properties within the same droplet, thus motivating finer temporal resolution of INP measurements in ~~the field~~
~~study, despite the increased labor intensity~~ field studies that desire the characterization of INP properties. Additionally, the level of N_{INP} after heat treatment (in red) also approximately followed the INP abundance classification (i.e., high-moderate-low), suggesting that the relative abundance of relatively heat-resistant INPs, i.e., mineral dust particles, although generally low in the background, may still explain the difference of N_{INP} in the selected samples.

~~Selected INP spectra for untreated, heated and storage conditions labeled high, moderate and low N_{INP} for case studies for impinger and PM10 samples. Note that the time stamps for the same N_{INP} labels regarding the impinger and PM10 samples are different. High INP cases: 11:05-12:05 UTC 21/10/2019 and 00:00-08:00 UTC 19/10/2019, moderate INP cases: 06:34-07:34 UTC 24/10/2019 and 16:00-24:00 UTC 21/10/2019, and low INP cases: 15:40-16:40 UTC 25/10/2019 and 00:00-08:00 UTC 23/10/2019 for impinger and PM10 samples, respectively.~~
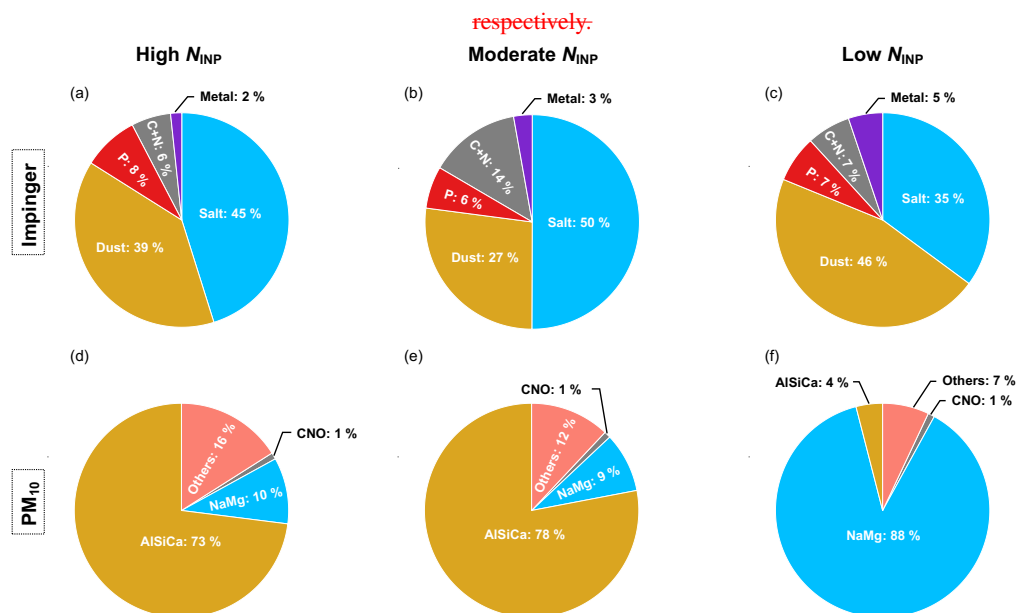
Figure 10. Normalized chemical composition fractions from SEM-EDX for selected (a), (b) and (c) impinger samples (droplet residuals), (d), (e) and (f) PM10 samples. Note that the categorization based on elemental compositions was slightly different for selected impinger (Cheng et al., 2022) and PM10 (Hiranuma et al., 2013) samples. The group C+N (CNO) include particles containing only carbon and nitrogen (and oxygen), mainly representative of (oxygenated) carbonaceous particles. The salt and NaMg classes are identical, composed of particles containing sodium and magnesium salts typically indicative of sea salt. The dust class is similar to AlSiCa except Al was not included in the categorization of dust in impinger droplet residual samples that were collected on aluminum substrates.

We evaluated the chemical compositions of the representative subset of droplet residual (impinger) and particular matter (PM10) filter samples labeled with high, moderate and low N_{INP} from offline ~~IN measurements ,~~ INP measurements in order to understand the diverse chemical compositions and sources (Figure. 10). Note ~~the~~ that the air masses cannot be compared directly from the compositions of the high, moderate, and low N_{INP} cases from the impinger and PM10 samples (Fig. 10) because they were not taken at the same time. Note the slight differences for classifications in impinger droplet residual and

PM$_{10}$ samples due to different probed elements (see detailed atomic fractions in Appendix D) and different sampling substrates.

545 C+N, P (Phosphorus), metal, dust, and salt are major compositions of impinger droplet residual samples (Figure 10 ~~(a), (b) and (c)~~a, b and c). The compositional diversity suggests that the sea salts and minerals sampled in our study could be aged ~~, and mixed, but~~ and mixed. Still, we cannot comment on the mixing state (internal vs. external) because all aerosols were sampled into the same liquid sample, allowing for post-sampling mixing. Abundant carbonaceous organics (C+N) were detected in the impinger_moderate sample, possibly released post to marine biological productions as suggested by the fluorescent signals

550 shown in Fig. 7 (b). Additionally, although higher dust and lower salt contents were detected in impinger_low samples, the INP concentration was low. A possible reason could be the suppression of ice nucleation activity of dust particles when aged in an aqueous environment (Kumar et al., 2018) in the impinger samples. Table 3 summarizes the detection of organic functional groups (bonds) for selected impinger droplet residual samples using Raman microspectroscopy. Organic-rich functional groups were identified in the high and moderate INP sample, associated with possible co-emission with marine biogenic aerosols as

555 previously discussed. In contrast, no organic functional groups were identified in the impinger_low sample.

Concerning PM$_{10}$ samples, greater dust (AlSiCa) content was associated with samples with higher N_{INP}, demonstrating major terrestrial sources. In contrast, more sea salt was pronounced in the low-N_{INP} sample. It remains unknown whether the abundance of INP of maritime origin is due to the presence of other marine constituents occasionally co-emitted with sea salt particles, such as sulfates or organic carbon, in the elevated particles during periods of marine biological activity.

560 To summarize, our single particle microspectroscopy results justify (1) the aerosol particle composition is not equivalent to the INP composition; (2) the variation in aerosol composition can infer the particle source and air mass history but cannot be a direct indicator of the INP abundance; and (3) quantitatively small organic compounds can substantially influence the INP prosperities at least in our studied samples collected in the Arctic.

Table 3. Summary of the number (#) of functional groups/chemical bonds detected via the Raman spectroscopy for selected impinger droplet residual samples.

Functional group/bond	Impinger_high (#)	Impinger_moderate (#)	Impinger_low (#)
Organic	13	12	< LOD[*]
Metal oxide(s)[**]	10	2	< LOD
Nitrogen bond(s)	3	5	< LOD
Aromatic ring(s)	4	3	< LOD
Total ~~NO.~~ # of spectra	13	12	< LOD

[*]Limit of detection.

[**]Possible interference from the aluminum foil that was used as sample substrate.

3.3.3 HYSPLIT backward trajectories for selected case studies

565 Backward trajectory analysis was conducted to assess the origin of sampled air masses and to identify potential long-range sources of the measured INPs in the Arctic coastal region in Ny-Ålesund. Figure 11 shows the air masses during the sampling

period of the impinger_high case originating from the coastal regions in the vicinity of Greenland, indicating possible influences from long-range transport of terrestrial sources, which qualitatively justifies the inclusion of some dust and organics. Similarly, rich organic and sea salt particles identified in the impinger_moderate sample could be attributed to the potential impacts from lower latitudes, where the residence time of air masses was much longer over the ice-free Barents and Kara Seas. A clear exception of air mass history was observed for the impinger_low sample when the air circulation within the Arctic circle was mostly over the ice pack or locally over Spitzbergen, which explains the low concentrations of INPs, organics and aerosol particles.
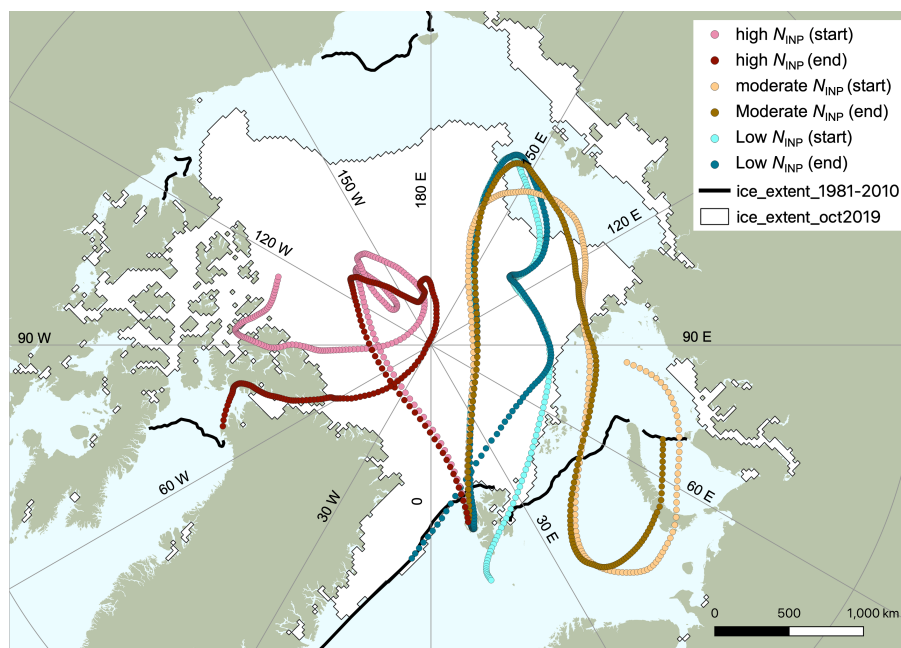
Figure 11. HYSPLIT backward trajectories over 10 days, starting at the sampling location at 5 m a.g.l height every hour within the sampling period (2 trajectories per sample), for the selected impinger INP case studies throughout the campaign. High INP case: 11:05 to 12:05 UTC 21/10/2019, moderate INP case: 06:34 to 07:34 UTC 24/10/2019 and low INP case: 15:40 to 16:40 UTC 25/10/2019.

Air mass trajectories during the sampling time of PM$_{10}$ filters (Figure 12) show that predominantly the trajectories were originated from western and northern Greenland in the high and moderate cases (Figures 12 a and b a and b), which coincided with relatively abundant INPs and high-latitude dust. These consistencies in high INPs and dust from Greenland for both PM$_{10}$ and impinger samples suggest that long-range transported dust from high latitudes (e.g., Greenland) could play an important role in the INP population in the remote Arctic regions.

28

Figure 12. HYSPLIT backward trajectories over 10 days, starting at the sampling location at 5 m a.g.l height every 2 hours (3 trajectories per sample), for the selected PM_{10} INP case studies throughout the campaign. High INP case from 00:00 to 08:00 UTC 19/10/2019, moderate INP case from 16:00 to 24:00 UTC 21/10/2019 and low INP case from 00:00 to 08:00 UTC 23/10/2019.

4   Summary and Conclusions

580   This study presents the measurement results of ambient INP concentrations and related aerosol properties during the NASCENT campaign in Ny-Ålesund, Svalbard in October-November 2019. A combination of online and offline INP measurement techniques were was applied in order to obtain a broad wider range of N_{INP}-T spectra and to understand the spatiotemporal variability of INPs from fine to coarse temporal resolutions. and aerosol size resolution. In this work, despite different INP concentrations being observed by the applied INP techniques (i.e., HINC, PM_{10}, impinger, and WT-CRAFT), all methods are

29

585 representative in the context of different properties of collected aerosols. A range of aerosol particle sizes can act as INPs so that different measurements are needed to cover the full-size range of aerosols smaller than 20 μm. This is true for particle size distribution measurements as well. PM_{10} filter and WT-CRAFT collect aerosol particles below 10 μm, and the impinger samples particles between 0.5 and 20 μm. A broader range of particle sizes measured by the combined methods allows for a better representation of ambient INPs. In addition, INP measurements from different approaches allow us to determine INP 590 properties from different species. For instance, if one focuses exclusively on mineral dust, a method is needed that captures the coarse-mode aerosol particles.

Overall, we observed that N_{INP} was approximately two orders of magnitudes lower compared to the global average (Petters and Wright, 2015) and was generally in good agreement with N_{INP} from previous studies in Ny-Ålesund. We showed that the majority of offline samples experienced a degradation in N_{INP} upon heat treatment, particularly towards warm temperatures 595 (i.e., $T > $ -15 °C), indicating the likely presence of proteinaceous or biogenic INPs. Correlation results linking aerosol properties to N_{INP} exhibited weak associations between N_{INP} and coarse-mode particles, despite their importance being highlighted by many previous studies. The averaging effect over relatively coarse-resolution data, scarcity of INPs and possible long-range modification processes were proposed as potential causes. Relatively strong correlations were found between N_{INP} and particle fluorescence, suggesting that highly IN-active bioaerosols, which may be inherently related to particles large in size during 600 the snow and ice-free season could serve as dominant local INP sources in the remote Arctic. The relationship between INP abundance and ocean-oriented high-speed wind and MSA concentrations further supports that N_{INP} could be contributed from locally enhanced SSA of biological origin.

Moreover, case studies with scenarios for a typical range of N_{INP} collected closer to the coast were presented (i.e., impinger samples at the aerosol container). The high N_{INP} case was associated with strong heat-lability, fluorescence, high wind speed 605 ~~of maritime origin~~originating from the ocean, elevated concentration of coarse-mode particles and surface area, and abundant organics. Chemical composition analyses reveal that the diversity in aerosol composition did not ~~have a substantial impact on~~ substantially impact the INP abundance, which could be a good future motivation to investigate the composition of cloud/ice residual and mixing state of aerosols and their associated impact on INP population and properties. Backward trajectories demonstrated possible high-latitude dust sources from long-range transport (e.g., coastal Greenland) that could be responsible 610 for the INP enrichment. In contrast, for low-N_{INP} cases, most of air mass history was experienced over the ice-pack zone. This research increased the data coverage of INP measurements in the remote Arctic and provided comprehensive analyses of the INP physicochemical properties and potential sources. Further studies ~~are needed in different seasons~~ with long-term observations are needed to elucidate the annual sources of INPs in the Arctic on a better statistical basis.

Appendix A: Assembly of frozen fractions with background and aerosol samples
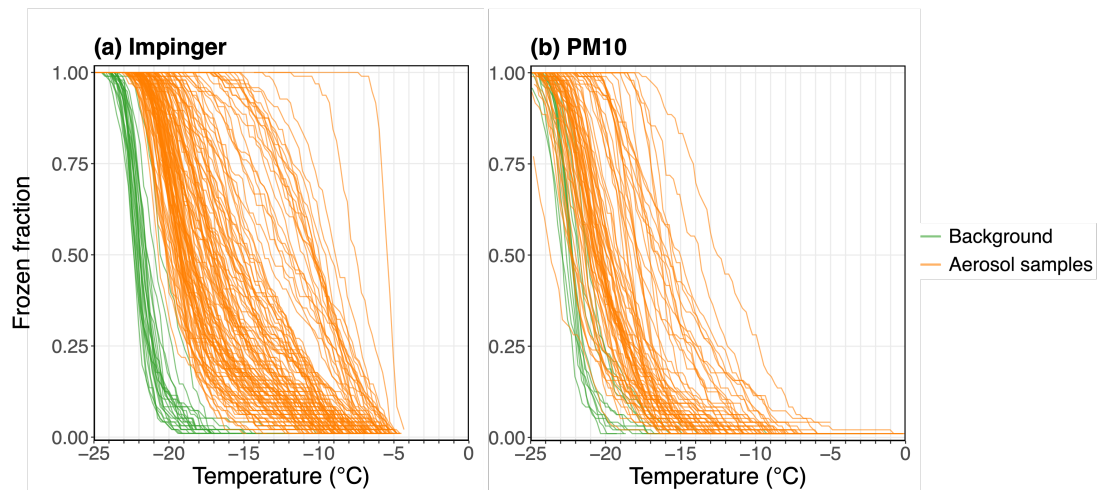
Figure A1. Assembly of frozen fraction curves as a function of temperature for aerosol samples and pure water reference experiments conducted with DRINCZ for all measurements from (a) impinger and (b) PM$_{10}$ samples.

Appendix B: Particle size distribution of case studies

Figure B1 provides full spectra of averaged particle size distribution within the time window for selected case studies presented in Figs. 7 and 8. The INPs collected by the impinger include only particles with aerodynamic diameters larger than 500 nm. Therefore, the high coarse-mode particle concentrations contributed to high INP case, but a few particles with diameters larger than approximately 8 μm, which were likely representative for instantaneously enhanced local sources, should explain the higher INP concentrations in impinger_moderate compared to impinger_low sample. Concerning PM$_{10}$ samples, the filters collected all particle sizes below 10 μm. The high INP concentration in PM10_high sample could be attributed to the high particle concentrations with D$_p$ > ca. 2.5 μm. However, compared to the PM10_low sample, particle loading in the PM10_moderate sample was comparable when D$_p$ > 2.5 μm, and were rather dominated by those under ca. 2.5 μm.
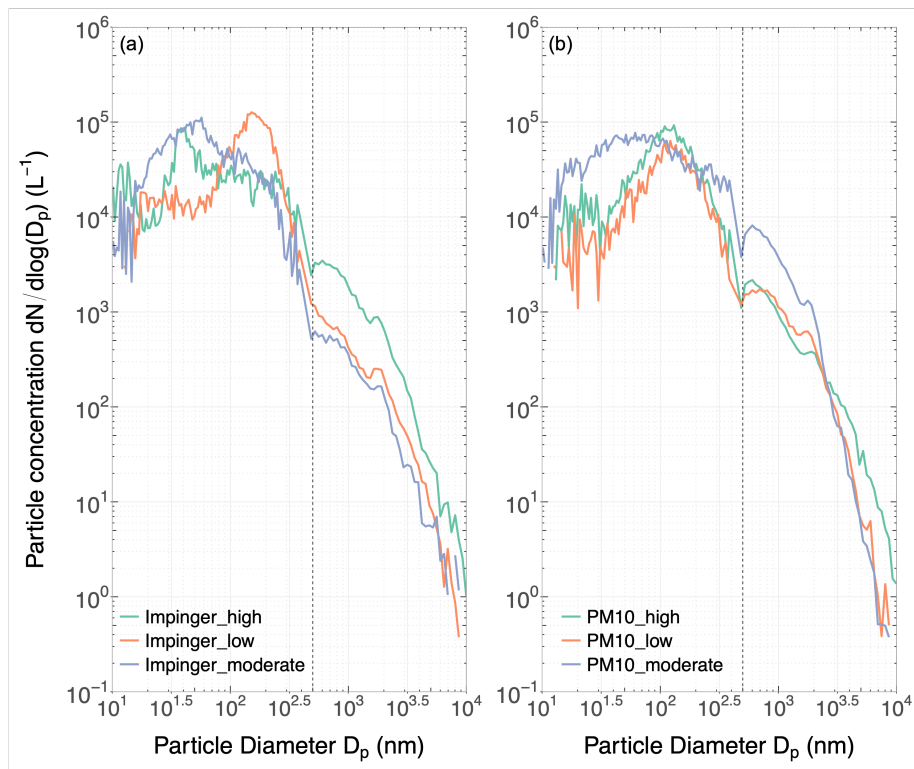
Figure B1. Average particle size distribution of selected cases of (a) impinger; and (b) PM_{10} sample. The vertical dashed lines indicate D_p = 500 nm, approximately the size boundary of SMPS and APS measurement.

Appendix C: SEM image of selected impinger samples
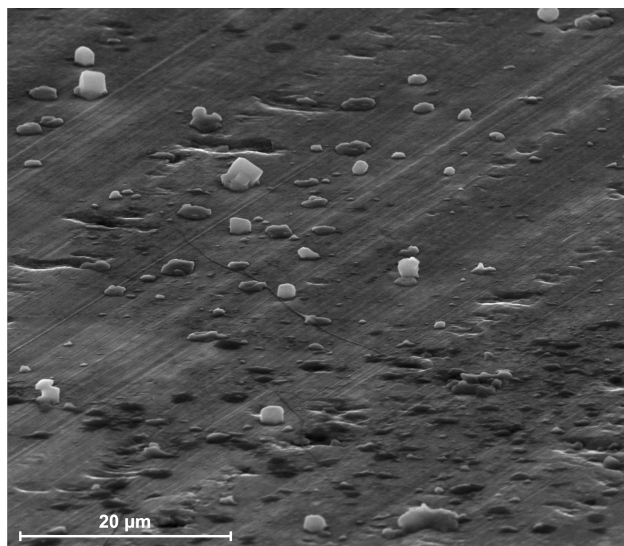
Figure C1. SEM image of impinger_high samples (in a tilted view). The image captures typical sea salt crystals analyzed by CCSEM-EDX. The CCSEM-EDX analysis covered a 0.5 by 0.5 mm area on the aluminum foil substrates to analyze sufficient particle population. All particles shown in the image above have therefore been analyzed by CCSEM-EDX.
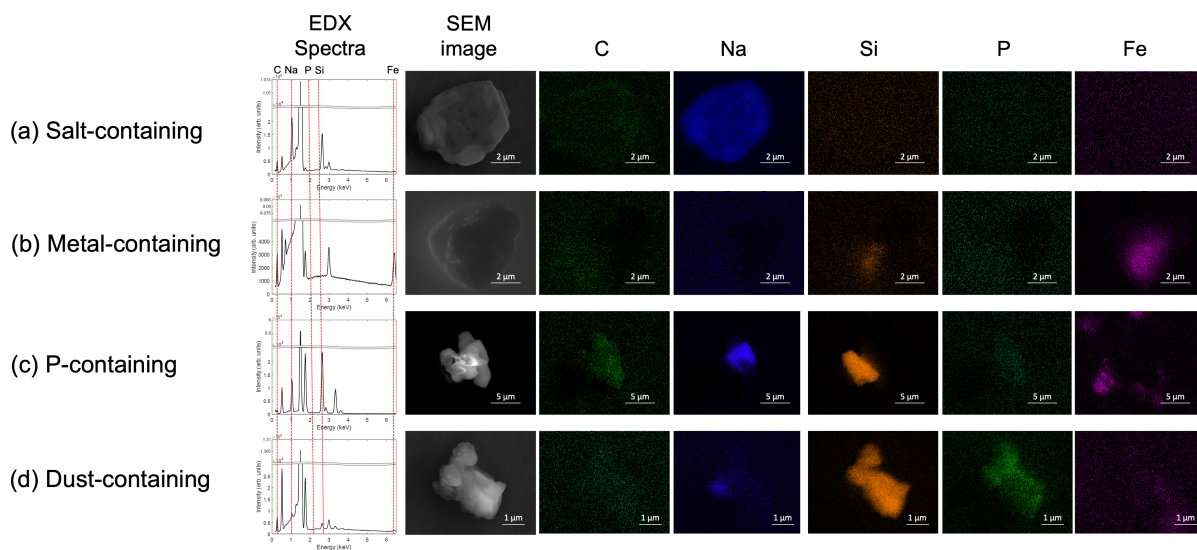
Figure C2. Representative SEM images of C, Na, Si, P, and Fe elemental maps and EDX spectra of (a) salt-containing particle, (b) metal-containing particle, (c) P-containing particle, and (d) dust-containing particle from impinger samples.

Appendix D: Atomic fraction for selected samples

Table D1. Atomic fraction of droplet residuals for selected impinger samples from CCSEM-EDX results.

Atoms	Impinger_high (%)	Impinger_moderate (%)	Impinger_low (%)
C	9.2±10.3	24.2±13.8	10.8±12.0
N	0.2±1.1	0.2±1.1	0.1±0.7
O	13.7±7.4	18.1±10.2	13.7±9.3
Na	20.9±22.9	9.2±11.0	7.8±8.5
Mg	14.0±7.1	18.4±7.1	15.3±9.1
Si	9.4±7.7	6.8±5.8	11.2±8.2
P	0.2±0.6	0.2±0.7	0.2±0.7
S	0.7±1.2	0.9±1.5	0.7±1.3
Ca	2.0±1.7	2.0±3.0	2.0±2.0
Mn	2.6±1.8	2.8±2.2	3.1±2.0
Fe	23.0±22.8	11.5±13.4	29.9±24.4
Zn	4.2±2.5	5.9±2.9	5.2±3.2

Table D2. Atomic fraction of particulate residuals for selected PM_{10} samples from SEM-EDX results.

Atoms	PM_{10}_high (%)	PM_{10}_moderate (%)	PM_{10}_low (%)
C	70.9±7.4	72.7±6.0	83.3±7.5
N	0.0±0.0	0.0±0.0	16.3±4.4
O	26.7±5.8	25.3±5.2	13.3±6.4
Na	0.6±0.4	0.5±0.5	1.7±1.1
Mg	1.3±1.6	0.6±0.4	0.5±0.3
Al	0.8±0.6	0.7±0.5	0.6±0.6
Si	1.0±1.1	1.0±0.8	1.6±2.4
P	0.1±0.0	0.1±0.1	0.0±0.0
S	0.3±0.3	0.5±0.5	0.2±0.2
Cl	0.2±0.2	0.1±0.2	0.8±0.6
K	0.2±0.2	0.1±0.1	0.1±0.0
Ca	0.5±0.5	0.4±0.5	0.1±0.1
Mn	0.2±0.2	0.1±0.0	0.0±0.0
Fe	0.7±0.7	0.4±0.5	0.3±0.1
Zn	0.1±0.0	0.1±0.0	0.1±0.0

References

Alsante, A. N., Thornton, D. C., and Brooks, S. D.: Ice nucleation catalyzed by the photosynthesis enzyme RuBisCO and other abundant biomolecules, Communications Earth & Environment, 4, 51, https://doi.org/10.1038/s43247-023-00707-7, 2023.

Barry, K. R., Hill, T. C., Moore, K. A., Douglas, T. A., Kreidenweis, S. M., DeMott, P. J., and Creamean, J. M.: Persistence and Potential Atmospheric Ramifications of Ice-Nucleating Particles Released from Thawing Permafrost, Environmental Science & Technology, 57, 3505–3515, https://doi.org/10.1021/acs.est.2c06530, 2023.

Beall, C. M., Lucero, D., Hill, T. C., DeMott, P. J., Stokes, M. D., and Prather, K. A.: Best practices for precipitation sample storage for offline studies of ice nucleation in marine and coastal environments, Atmospheric Measurement Techniques, 13, 6473–6486, https://doi.org/https://doi.org/10.5194/amt-13-6473-2020, 2020.

Becagli, S., Ghedini, C., Peeters, S., Rottiers, A., Traversi, R., Udisti, R., Chiari, M., Jalba, A., Despiau, S., Dayan, U., and Temara, A.: MBAS (Methylene Blue Active Substances) and LAS (Linear Alkylbenzene Sulphonates) in Mediterranean coastal aerosols: Sources and transport processes, Atmospheric Environment, 45, 6788–6801, https://doi.org/10.1016/j.atmosenv.2011.04.041, 2011.

Becagli, S., Amore, A., Caiazzo, L., Iorio, T. D., Sarra, A. d., Lazzara, L., Marchese, C., Meloni, D., Mori, G., Muscari, G., Nuccio, C., Pace, G., Severi, M., and Traversi, R.: Biogenic Aerosol in the Arctic from Eight Years of MSA Data from Ny Ålesund (Svalbard Islands) and Thule (Greenland), Atmosphere, 10, https://doi.org/10.3390/atmos10070349, 2019.

Bintanja, R., Van der Linden, E., and Hazeleger, W.: Boundary layer stability and Arctic climate change: A feedback study using EC-Earth, Climate dynamics, 39, 2659–2673, https://doi.org/https://doi.org/10.1007/s00382-011-1272-1, 2012.

Cheng, Z., Morgenstern, M., Zhang, B., Fraund, M., Lata, N. N., Brimberry, R., Marcus, M. A., Mazzoleni, L., Fialho, P., Henning, S., Wehner, B., Mazzoleni, C., and China, S.: Particle phase-state variability in the North Atlantic free troposphere during summertime is determined by atmospheric transport patterns and sources, Atmospheric Chemistry and Physics, 22, 9033–9057, https://doi.org/10.5194/acp-22-9033-2022, 2022.

Chou, C., Kanji, Z. A., Stetzer, O., Tritscher, T., Chirico, R., Heringa, M. F., Weingartner, E., Prévôt, A. S. H., Baltensperger, U., and Lohmann, U.: Effect of photochemical ageing on the ice nucleation properties of diesel and wood burning particles, Atmospheric Chemistry and Physics, 13, 761–772, https://doi.org/10.5194/acp-13-761-2013, 2013.

Conen, F., Stopelli, E., and Zimmermann, L.: Clues that decaying leaves enrich Arctic air with ice nucleating particles, Atmospheric environment, 129, 91–94, https://doi.org/https://doi.org/10.1016/j.atmosenv.2016.01.027, 2016.

Creamean, J. M., Cross, J. N., Pickart, R., McRaven, L., Lin, P., Pacini, A., Hanlon, R., Schmale, D. G., Ceniceros, J., Aydell, T., Colombi, N., Bolger, E., and DeMott, P. J.: Ice nucleating particles carried from below a phytoplankton bloom to the Arctic atmosphere, Geophysical Research Letters, 46, 8572–8581, https://doi.org/https://doi.org/10.1029/2019GL083039, 2019.

Creamean, J. M., Hill, T. C., DeMott, P. J., Uetake, J., Kreidenweis, S., and Douglas, T. A.: Thawing permafrost: an overlooked source of seeds for Arctic cloud formation, Environmental Research Letters, 15, 084 022, https://doi.org/https://doi.org/10.1088/1748-9326/ab87d3, 2020.

Creamean, J. M., Ceniceros, J. E., Newman, L., Pace, A. D., Hill, T. C. J., DeMott, P. J., and Rhodes, M. E.: Evaluating the potential for Haloarchaea to serve as ice nucleating particles, Biogeosciences, 18, 3751–3762, https://doi.org/10.5194/bg-18-3751-2021, 2021.

David, R. O., Cascajo-Castresana, M., Brennan, K. P., Rösch, M., Els, N., Werz, J., Weichlinger, V., Boynton, L. S., Bogler, S., Borduas-Dedekind, N., Marcolli, C., and Kanji, Z. A.: Development of the DRoplet Ice Nuclei Counter Zurich (DRINCZ): Validation and applica-

tion to field-collected snow samples, Atmospheric Measurement Techniques, 12, 6865–6888, https://doi.org/10.5194/amt-12-6865-2019, 2019.

685 DeMott, P. J., Prenni, A. J., Liu, X., Kreidenweis, S. M., Petters, M. D., Twohy, C. H., Richardson, M. S., Eidhammer, T., and Rogers, D. C.: Predicting global atmospheric ice nuclei distributions and their impacts on climate, Proceedings of the National Academy of Sciences of the United States of America, 107, 11 217–11 222, https://doi.org/10.1073/pnas.0910818107, 2010.

DeMott, P. J., Prenni, A. J., McMeeking, G. R., Sullivan, R. C., Petters, M. D., Tobo, Y., Niemand, M., Möhler, O., Snider, J. R., Wang, Z., and Kreidenweis, S. M.: Integrating laboratory and field data to quantify the immersion freezing ice nucleation activity of mineral dust
690 particles, Atmospheric Chemistry and Physics, 15, 393–409, https://doi.org/10.5194/acp-15-393-2015, 2015.

DeMott, P. J., Hill, T. C. J., McCluskey, C. S., Prather, K. A., Collins, D. B., Sullivan, R. C., Ruppel, M. J., Mason, R. H., Irish, V. E., Lee, T., Hwang, C. Y., Rhee, T. S., Snider, J. R., McMeeking, G. R., Dhaniyala, S., Lewis, E. R., Wentzell, J. J. B., Abbatt, J., Lee, C., Sultana, C. M., Ault, A. P., Axson, J. L., Martinez, M. D., Venero, I., Santos-Figueroa, G., Stokes, M. D., Deane, G. B., Mayol-Bracero, O. L., Grassian, V. H., Bertram, T. H., Bertram, A. K., Moffett, B. F., and Franc, G. D.: Sea spray aerosol as a unique source of ice nucleating particles,
695 Proceedings of the National Academy of Sciences, 113, 5797–5803, https://doi.org/www.pnas.org/cgi/doi/10.1073/pnas.1514034112, 2016.

Deng, C., Brooks, S. D., Vidaurre, G., and Thornton, D. C. O.: Using Raman Microspectroscopy to Determine Chemical Composition and Mixing State of Airborne Marine Aerosols over the Pacific Ocean, Aerosol Science and Technology, 48, 193–206, https://doi.org/10.1080/02786826.2013.867297, 2014.

700 Eirund, G. K., Possner, A., and Lohmann, U.: Response of Arctic mixed-phase clouds to aerosol perturbations under different surface forcings, Atmospheric Chemistry and Physics, 19, 9847–9864, https://doi.org/https://doi.org/10.5194/acp-19-9847-2019, 2019.

Forster, P., Storelvmo, T., Armour, K., Collins, W., Dufresne, J.-L., Frame, D., Lunt, D., Mauritsen, T., Palmer, M., Watanabe, M., et al.: The Earth's energy budget, climate feedbacks, and climate sensitivity, Climate Change 2021: The Physical Science Basis. Contribution of Working Group I to the Sixth Assessment Report of the Intergovernmental Panel on Climate Change, 2021.

705 Friedman, B., Kulkarni, G., Beránek, J., Zelenyuk, A., Thornton, J. A., and Cziczo, D. J.: Ice nucleation and droplet formation by bare and coated soot particles, Journal of Geophysical Research: Atmospheres, 116, https://doi.org/10.1029/2011JD015999, 2011.

Gilardoni, S., Lupi, A., Mazzola, M., Cappelletti, D. M., Moroni, B., Ferrero, L., Markuszewski, P., Rozwadowska, A., Krejci, R., Zieger, P., et al.: Atmospheric black carbon in Svalbard (ABC Svalbard), SESS report, pp. 200–201, 2019.

Gong, X., Wex, H., Voigtländer, J., Fomba, K. W., Weinhold, K., van Pinxteren, M., Henning, S., Müller, T., Herrmann, H., and Stratmann,
710 F.: Characterization of aerosol particles at Cabo Verde close to sea level and at the cloud level – Part 1: Particle number size distribution, cloud condensation nuclei and their origins, Atmospheric Chemistry and Physics, 20, 1431–1449, https://doi.org/10.5194/acp-20-1431-2020, 2020.

Graversen, R. G. and Wang, M.: Polar amplification in a coupled climate model with locked albedo, Climate Dynamics, 33, 629–643, https://doi.org/https://doi.org/10.1007/s00382-009-0535-6, 2009.

715 Hall, A.: The Role of Surface Albedo Feedback in Climate, Journal of Climate, 17, 1550 – 1568, https://doi.org/10.1175/1520-0442(2004)017<1550:TROSAF>2.0.CO;2, 2004.

Hande, L. B. and Hoose, C.: Partitioning the primary ice formation modes in large eddy simulations of mixed-phase clouds, Atmospheric Chemistry and Physics, 17, 14 105–14 118, https://doi.org/10.5194/acp-17-14105-2017, 2017.

Harrington, J. Y. and Olsson, P. Q.: On the potential influence of ice nuclei on surface-forced marine stratocumulus cloud dynamics, Journal
720 of Geophysical Research: Atmospheres, 106, 27 473–27 484, https://doi.org/10.1029/2000JD000236, 2001.

Harrington, J. Y., Reisin, T., Cotton, W. R., and Kreidenweis, S. M.: Cloud resolving simulations of Arctic stratus: Part II: Transition-season clouds, Atmospheric Research, 51, 45–75, https://doi.org/10.1016/S0169-8095(98)00098-2, 1999.

Hartigan, J. A. and Wong, M. A.: Algorithm AS 136: A K-Means Clustering Algorithm, Journal of the Royal Statistical Society. Series C (Applied Statistics), 28, 100–108, http://www.jstor.org/stable/2346830, 1979.

725 Hartmann, M., Adachi, K., Eppers, O., Haas, C., Herber, A., Holzinger, R., Hünerbein, A., Jäkel, E., Jentzsch, C., van Pinxteren, M., Wex, H., Willmes, S., and Stratmann, F.: Wintertime airborne measurements of ice nucleating particles in the high Arctic: A hint to a marine, biogenic source for ice nucleating particles, Geophysical Research Letters, 47, e2020GL087770, https://doi.org/https://doi.org/10.1029/2020GL087770, 2020.

Hawker, R. E., Miltenberger, A. K., Wilkinson, J. M., Hill, A. A., Shipway, B. J., Cui, Z., Cotton, R. J., Carslaw, K. S., Field, P. R., and
730 Murray, B. J.: The temperature dependence of ice-nucleating particle concentrations affects the radiative properties of tropical convective cloud systems, Atmospheric Chemistry and Physics, 21, 5439–5461, https://doi.org/https://doi.org/10.5194/acp-21-5439-2021, 2021.

Hill, T. C. J., DeMott, P. J., Tobo, Y., Fröhlich-Nowoisky, J., Moffett, B. F., Franc, G. D., and Kreidenweis, S. M.: Sources of organic ice nucleating particles in soils, Atmospheric Chemistry and Physics, 16, 7195–7211, https://doi.org/10.5194/acp-16-7195-2016, 2016.

Hines, K. M., Bromwich, D. H., Silber, I., Russell, L. M., and Bai, L.: Predicting Frigid Mixed-Phase Clouds for Pristine Coastal Antarc-
735 tica, Journal of Geophysical Research: Atmospheres, 126, e2021JD035112, https://doi.org/10.1029/2021JD035112, e2021JD035112 2021JD035112, 2021.

Hiranuma, N., Brooks, S. D., Moffet, R. C., Glen, A., Laskin, A., Gilles, M. K., Liu, P., Macdonald, A. M., Strapp, J. W., and McFarquhar, G. M.: Chemical characterization of individual particles and residuals of cloud droplets and ice crystals collected on board research aircraft in the ISDAC 2008 study, Journal of Geophysical Research: Atmospheres, 118, 6564–6579, https://doi.org/10.1002/jgrd.50484, 2013.

740 Hiranuma, N., Adachi, K., Bell, D. M., Belosi, F., Beydoun, H., Bhaduri, B., Bingemer, H., Budke, C., Clemen, H.-C., Conen, F., Cory, K. M., Curtius, J., DeMott, P. J., Eppers, O., Grawe, S., Hartmann, S., Hoffmann, N., Höhler, K., Jantsch, E., Kiselev, A., Koop, T., Kulkarni, G., Mayer, A., Murakami, M., Murray, B. J., Nicosia, A., Petters, M. D., Piazza, M., Polen, M., Reicher, N., Rudich, Y., Saito, A., Santachiara, G., Schiebel, T., Schill, G. P., Schneider, J., Segev, L., Stopelli, E., Sullivan, R. C., Suski, K., Szakáll, M., Tajiri, T., Taylor, H., Tobo, Y., Ullrich, R., Weber, D., Wex, H., Whale, T. F., Whiteside, C. L., Yamashita, K., Zelenyuk, A., and Möhler, O.: A
745 comprehensive characterization of ice nucleation by three different types of cellulose particles immersed in water, Atmospheric Chemistry and Physics, 19, 4823–4849, https://doi.org/10.5194/acp-19-4823-2019, 2019.

Hoose, C. and Möhler, O.: Heterogeneous ice nucleation on atmospheric aerosols: a review of results from laboratory experiments, Atmospheric Chemistry and Physics, 12, 9817–9854, https://doi.org/https://doi.org/10.5194/acp-12-9817-2012, 2012.

Ickes, L., Porter, G. C. E., Wagner, R., Adams, M. P., Bierbauer, S., Bertram, A. K., Bilde, M., Christiansen, S., Ekman, A. M. L., Gorokhova,
750 E., Höhler, K., Kiselev, A. A., Leck, C., Möhler, O., Murray, B. J., Schiebel, T., Ullrich, R., and Salter, M. E.: The ice-nucleating activity of Arctic sea surface microlayer samples and marine algal cultures, Atmospheric Chemistry and Physics, 20, 11089–11117, https://doi.org/10.5194/acp-20-11089-2020, 2020.

Inoue, J., Tobo, Y., Taketani, F., and Sato, K.: Oceanic Supply of Ice-Nucleating Particles and Its Effect on Ice Cloud Formation: A Case Study in the Arctic Ocean During a Cold-Air Outbreak in Early Winter, Geophysical Research Letters, 48, e2021GL094646,
755 https://doi.org/10.1029/2021GL094646, e2021GL094646 2021GL094646, 2021.

Intrieri, J. M., Shupe, M. D., Uttal, T., and McCarty, B. J.: An annual cycle of Arctic cloud characteristics observed by radar and lidar at SHEBA, Journal of Geophysical Research: Oceans, 107, SHE 5–1–SHE 5–15, https://doi.org/10.1029/2000JC000423, 2002.

Irish, V. E., Elizondo, P., Chen, J., Chou, C., Charette, J., Lizotte, M., Ladino, L. A., Wilson, T. W., Gosselin, M., Murray, B. J., et al.: Ice-nucleating particles in Canadian Arctic sea-surface microlayer and bulk seawater, Atmospheric Chemistry and Physics, 17, 10 583–10 595, https://doi.org/10.5194/acp-17-10583-2017, 2017.

Jiang, H., Cotton, W. R., Pinto, J. O., Curry, J. A., and Weissbluth, M. J.: Cloud Resolving Simulations of Mixed-Phase Arctic Stratus Observed during BASE: Sensitivity to Concentration of Ice Crystals and Large-Scale Heat and Moisture Advection, Journal of the Atmospheric Sciences, 57, 2105 – 2117, https://doi.org/10.1175/1520-0469(2000)057<2105:CRSOMP>2.0.CO;2, 2000.

Kanji, Z. A., Ladino, L. A., Wex, H., Boose, Y., Burkert-Kohn, M., Cziczo, D. J., and Krämer, M.: Overview of ice nucleating particles, Meteorological Monographs, 58, 1–1, https://doi.org/10.1175/AMSMONOGRAPHS-D-16-0006.1, 2017.

Kanji, Z. A., Welti, A., Corbin, J. C., and Mensah, A. A.: Black Carbon Particles Do Not Matter for Immersion Mode Ice Nucleation, Geophysical Research Letters, 47, e2019GL086 764, https://doi.org/10.1029/2019GL086764, e2019GL086764 2019GL086764, 2020.

Kodinariya, T. M. and Makwana, P. R.: Review on determining number of Cluster in K-Means Clustering, International Journal, 1, 90–95, https://www.researchgate.net/profile/Trupti-Kodinariya/publication/313554124_Review_on_Determining_of_Cluster_in_K-means_Clustering/links/5789fda408ae59aa667931d2/Review-on-Determining-of-Cluster-in-K-means-Clustering.pdf, 2013.

Korolev, A., McFarquhar, G., Field, P. R., Franklin, C., Lawson, P., Wang, Z., Williams, E., Abel, S. J., Axisa, D., Borrmann, S., Crosier, J., Fugal, J., Krämer, M., Lohmann, U., Schlenczek, O., Schnaiter, M., and Wendisch, M.: Mixed-Phase Clouds: Progress and Challenges, Meteorological Monographs, 58, 5.1 – 5.50, https://doi.org/10.1175/AMSMONOGRAPHS-D-17-0001.1, 2017.

Korolev, A., Heckman, I., Wolde, M., Ackerman, A. S., Fridlind, A. M., Ladino, L. A., Lawson, R. P., Milbrandt, J., and Williams, E.: A new look at the environmental conditions favorable to secondary ice production, Atmospheric Chemistry and Physics, 20, 1391–1429, https://doi.org/10.5194/acp-20-1391-2020, 2020.

Kumar, A., Marcolli, C., Luo, B., and Peter, T.: Ice nucleation activity of silicates and aluminosilicates in pure water and aqueous solutions – Part 1: The K-feldspar microcline, Atmospheric Chemistry and Physics, 18, 7057–7079, https://doi.org/10.5194/acp-18-7057-2018, 2018.

Kupiszewski, P., Zanatta, M., Mertes, S., Vochezer, P., Lloyd, G., Schneider, J., Schenk, L., Schnaiter, M., Baltensperger, U., Weingartner, E., and Gysel, M.: Ice residual properties in mixed-phase clouds at the high-alpine Jungfraujoch site, Journal of Geophysical Research: Atmospheres, 121, 12,343–12,362, https://doi.org/10.1002/2016JD024894, 2016.

Lacher, L., Lohmann, U., Boose, Y., Zipori, A., Herrmann, E., Bukowiecki, N., Steinbacher, M., and Kanji, Z. A.: The Horizontal Ice Nucleation Chamber (HINC): INP measurements at conditions relevant for mixed-phase clouds at the High Altitude Research Station Jungfraujoch, Atmospheric Chemistry and Physics, 17, 15 199–15 224, https://doi.org/10.5194/acp-17-15199-2017, 2017.

Lacher, L., Steinbacher, M., Bukowiecki, N., Herrmann, E., Zipori, A., and Kanji, Z. A.: Impact of Air Mass Conditions and Aerosol Properties on Ice Nucleating Particle Concentrations at the High Altitude Research Station Jungfraujoch, Atmosphere, 9, https://doi.org/10.3390/atmos9090363, 2018.

Larkin, P.: Infrared and Raman spectroscopy: principles and spectral interpretation, Elsevier, 2017.

Laskin, A., Cowin, J., and Iedema, M.: Analysis of individual environmental particles using modern methods of electron microscopy and X-ray microanalysis, Journal of Electron Spectroscopy and Related Phenomena, 150, 260–274, https://doi.org/10.1016/j.elspec.2005.06.008, science and Spectroscopy of Environmentally Important Interfaces, 2006.

Lata, N. N., Zhang, B., Schum, S., Mazzoleni, L., Brimberry, R., Marcus, M. A., Cantrell, W. H., Fialho, P., Mazzoleni, C., and China, S.: Aerosol Composition, Mixing State, and Phase State of Free Tropospheric Particles and Their Role in Ice Cloud Formation, ACS Earth and Space Chemistry, 5, 3499–3510, https://doi.org/10.1021/acsearthspacechem.1c00315, 2021.

795 Lewis, E. R., Lewis, R., and Schwartz, S. E.: Sea salt aerosol production: mechanisms, methods, measurements, and models, vol. 152, American geophysical union, 2004.

Li, G., Wieder, J., Pasquier, J. T., Henneberger, J., and Kanji, Z. A.: Predicting atmospheric background number concentration of ice nucleating particles in the Arctic, Atmospheric Chemistry and Physics Discussions, 2022, 1–27, https://doi.org/10.5194/acp-2022-21, 2022.

Lohmann, U.: Possible Aerosol Effects on Ice Clouds via Contact Nucleation, Journal of the Atmospheric Sciences, 59, 647 – 656,
800 https://doi.org/10.1175/1520-0469(2001)059<0647:PAEOIC>2.0.CO;2, 2002.

Lohmann, U. and Neubauer, D.: The importance of mixed-phase and ice clouds for climate sensitivity in the global aerosol–climate model ECHAM6-HAM2, Atmospheric Chemistry and Physics, 18, 8807–8828, https://doi.org/10.5194/acp-18-8807-2018, 2018.

Mahrt, F., Marcolli, C., David, R. O., Grönquist, P., Barthazy Meier, E. J., Lohmann, U., and Kanji, Z. A.: Ice nucleation abilities of soot particles determined with the Horizontal Ice Nucleation Chamber, Atmospheric Chemistry and Physics, 18, 13 363–13 392,
805 https://doi.org/10.5194/acp-18-13363-2018, 2018.

Mason, R., Si, M., Chou, C., Irish, V., Dickie, R., Elizondo, P., Wong, R., Brintnell, M., Elsasser, M., Lassar, W., et al.: Size-resolved measurements of ice-nucleating particles at six locations in North America and one in Europe, Atmospheric Chemistry and Physics, 16, 1637–1651, https://doi.org/https://doi.org/10.5194/acp-16-1637-2016, 2016.

Mazzola, M., Viola, A. P., Lanconelli, C., and Vitale, V.: Atmospheric observations at the Amundsen-Nobile climate change tower in Ny-
810 Ålesund, Svalbard, Rendiconti Lincei, 27, 7–18, https://doi.org/https://doi.org/10.1007/s12210-016-0540-8, 2016.

McCluskey, C. S., Ovadnevaite, J., Rinaldi, M., Atkinson, J., Belosi, F., Ceburnis, D., Marullo, S., Hill, T. C., Lohmann, U., Kanji, Z. A., O'Dowd, C., Kreidenweis, S. M., and DeMott, P. J.: Marine and Terrestrial Organic Ice-Nucleating Particles in Pristine Marine to Continentally Influenced Northeast Atlantic Air Masses, Journal of Geophysical Research: Atmospheres, 123, 6196–6212, https://doi.org/10.1029/2017JD028033, 2018.

815 Moallemi, A., Landwehr, S., Robinson, C., Simó, R., Zamanillo, M., Chen, G., Baccarini, A., Schnaiter, M., Henning, S., Modini, R. L., Gysel-Beer, M., and Schmale, J.: Sources, Occurrence and Characteristics of Fluorescent Biological Aerosol Particles Measured Over the Pristine Southern Ocean, Journal of Geophysical Research: Atmospheres, 126, e2021JD034 811, https://doi.org/10.1029/2021JD034811, 2021.

Morrison, H., De Boer, G., Feingold, G., Harrington, J., Shupe, M. D., and Sulia, K.: Resilience of persistent Arctic mixed-phase clouds,
820 Nature Geoscience, 5, 11–17, https://doi.org/https://doi.org/10.1038/ngeo1332, 2012.

Murray, B., O'sullivan, D., Atkinson, J., and Webb, M.: Ice nucleation by particles immersed in supercooled cloud droplets, Chemical Society Reviews, 41, 6519–6554, https://doi.org/https://doi.org/10.1039/C2CS35200A, 2012.

Murray, B. J., Carslaw, K. S., and Field, P. R.: Opinion: Cloud-phase climate feedback and the importance of ice-nucleating particles, Atmospheric Chemistry and Physics, 21, 665–679, https://doi.org/https://doi.org/10.5194/acp-21-665-2021, 2021.

825 Paramonov, M., Drossaart van Dusseldorp, S., Gute, E., Abbatt, J. P. D., Heikkilä, P., Keskinen, J., Chen, X., Luoma, K., Heikkinen, L., Hao, L., Petäjä, T., and Kanji, Z. A.: Condensation/immersion mode ice-nucleating particles in a boreal environment, Atmospheric Chemistry and Physics, 20, 6687–6706, https://doi.org/10.5194/acp-20-6687-2020, 2020.

Pasquier, J. T., David, R. O., Freitas, G., Gierens, R., Gramlich, Y., Haslett, S., Li, G., Schäfer, B., Siegel, K., Wieder, J., Adachi, K., Belosi, F., Carlsen, T., Decesari, S., Ebell, K., Gilardoni, S., Gysel-Beer, M., Henneberger, J., Inoue, J., Kanji, Z. A., Koike, M., Kondo, Y.,
830 Krejci, R., Lohmann, U., Maturilli, M., Mazzolla, M., Modini, R., Mohr, C., Motos, G., Nenes, A., Nicosia, A., Ohata, S., Paglione, M., Park, S., Pileci, R. E., Ramelli, F., Rinaldi, M., Ritter, C., Sato, K., Storelvmo, T., Tobo, Y., Traversi, R., Viola, A., and Zieger, P.:

The Ny-Ålesund Aerosol Cloud Experiment (NASCENT): Overview and First Results, Bulletin of the American Meteorological Society, https://doi.org/10.1175/BAMS-D-21-0034.1, 2022a.

Pasquier, J. T., Henneberger, J., Ramelli, F., Lauber, A., David, R. O., Wieder, J., Carlsen, T., Gierens, R., Maturilli, M., and Lohmann, U.:
835   Conditions favorable for secondary ice production in Arctic mixed-phase clouds, Atmospheric Chemistry and Physics, 22, 15 579–15 601, https://doi.org/10.5194/acp-22-15579-2022, 2022b.

Perring, A. E., Schwarz, J. P., Baumgardner, D., Hernandez, M. T., Spracklen, D. V., Heald, C. L., Gao, R. S., Kok, G., McMeeking, G. R., McQuaid, J. B., and Fahey, D. W.: Airborne observations of regional variation in fluorescent aerosol across the United States, Journal of Geophysical Research: Atmospheres, 120, 1153–1170, https://doi.org/10.1002/2014JD022495, 2015.

840   Petters, M. and Wright, T.: Revisiting ice nucleation from precipitation samples, Geophysical Research Letters, 42, 8758–8766, https://doi.org/https://doi.org/10.1002/2015GL065733, 2015.

Pithan, F. and Mauritsen, T.: Arctic amplification dominated by temperature feedbacks in contemporary climate models, Nature Geoscience, 7, 181, https://doi.org/10.1038/ngeo2071, 2014.

Pöhlker, C., Huffman, J. A., and Pöschl, U.: Autofluorescence of atmospheric bioaerosols – fluorescent biomolecules and potential interfer-
845   ences, Atmospheric Measurement Techniques, 5, 37–71, https://doi.org/10.5194/amt-5-37-2012, 2012.

Porter, G. C. E., Adams, M. P., Brooks, I. M., Ickes, L., Karlsson, L., Leck, C., Salter, M. E., Schmale, J., Siegel, K., Sikora, S. N. F., Tarn, M. D., Füllers, J., Wernli, H., Zieger, P., Zinke, J., and Murray, B. J.: Highly Active Ice-Nucleating Particles at the Summer North Pole, Journal of Geophysical Research: Atmospheres, 127, e2021JD036 059, https://doi.org/10.1029/2021JD036059, e2021JD036059 2021JD036059, 2022.

850   Pummer, B. G., Budke, C., Augustin-Bauditz, S., Niedermeier, D., Felgitsch, L., Kampf, C. J., Huber, R. G., Liedl, K. R., Loerting, T., Moschen, T., Schauperl, M., Tollinger, M., Morris, C. E., Wex, H., Grothe, H., Pöschl, U., Koop, T., and Fröhlich-Nowoisky, J.: Ice nucleation by water-soluble macromolecules, Atmospheric Chemistry and Physics, 15, 4077–4091, https://doi.org/10.5194/acp-15-4077-2015, 2015.

Rinaldi, M., Hiranuma, N., Santachiara, G., Mazzola, M., Mansour, K., Paglione, M., Rodriguez, C. A., Traversi, R., Becagli, S., Cappelletti,
855   D., et al.: Ice-nucleating particle concentration measurements from Ny-Ålesund during the Arctic spring–summer in 2018, Atmospheric Chemistry and Physics, 21, 14 725–14 748, https://doi.org/https://doi.org/10.5194/acp-21-14725-2021, 2021.

Rolph, G., Stein, A., and Stunder, B.: Real-time Environmental Applications and Display sYstem: READY, Environmental Modelling & Software, 95, 210–228, https://doi.org/10.1016/j.envsoft.2017.06.025, 2017.

Sanchez-Marroquin, A., Arnalds, O., Baustian-Dorsi, K. J., Browse, J., Dagsson-Waldhauserova, P., Harrison, A. D., Maters, E. C., Pringle,
860   K. J., Vergara-Temprado, J., Burke, I. T., McQuaid, J. B., Carslaw, K. S., and Murray, B. J.: Iceland is an episodic source of atmospheric ice-nucleating particles relevant for mixed-phase clouds, Science Advances, 6, eaba8137, https://doi.org/10.1126/sciadv.aba8137, 2020.

Savage, N. J., Krentz, C. E., Könemann, T., Han, T. T., Mainelis, G., Pöhlker, C., and Huffman, J. A.: Systematic characterization and fluorescence threshold strategies for the wideband integrated bioaerosol sensor (WIBS) using size-resolved biological and interfering particles, Atmospheric Measurement Techniques, 10, 4279–4302, https://doi.org/10.5194/amt-10-4279-2017, 2017.

865   Schmale, J., Zieger, P., and Ekman, A. M.: Aerosols in current and future Arctic climate, Nature Climate Change, 11, 95–105, https://doi.org/10.1038/s41558-020-00969-5, 2021.

Schneider, J., Höhler, K., Heikkilä, P., Keskinen, J., Bertozzi, B., Bogert, P., Schorr, T., Umo, N. S., Vogel, F., Brasseur, Z., et al.: The seasonal cycle of ice-nucleating particles linked to the abundance of biogenic aerosol in boreal forests, Atmospheric Chemistry and Physics, 21, 3899–3918, https://doi.org/https://doi.org/10.5194/acp-21-3899-2021, 2021.

870   Schrod, J., Thomson, E. S., Weber, D., Kossmann, J., Pöhlker, C., Saturno, J., Ditas, F., Artaxo, P., Clouard, V., Saurel, J.-M., et al.: Long-term deposition and condensation ice-nucleating particle measurements from four stations across the globe, Atmospheric Chemistry and Physics, 20, 15 983–16 006, https://doi.org/https://doi.org/10.5194/acp-20-15983-2020, 2020.

Screen, J. A. and Simmonds, I.: The central role of diminishing sea ice in recent Arctic temperature amplification, Nature, 464, 1334–1337, https://doi.org/https://doi.org/10.1038/nature09051, 2010.

875   Seifried, T. M., Reyzek, F., Bieber, P., and Grothe, H.: Scots Pines (Pinus sylvestris) as Sources of Biological Ice-Nucleating Macromolecules (INMs), Atmosphere, 14, https://doi.org/10.3390/atmos14020266, 2023.

Serreze, M. C. and Barry, R. G.: Processes and impacts of Arctic amplification: A research synthesis, Global and planetary change, 77, 85–96, https://doi.org/10.1016/j.gloplacha.2011.03.004, 2011.

Serreze, M. C., Holland, M. M., and Stroeve, J.: Perspectives on the Arctic's Shrinking Sea-Ice Cover, Science, 315, 1533–1536,
880   https://doi.org/10.1126/science.1139426, 2007.

Sinha, P. R., Kondo, Y., Koike, M., Ogren, J. A., Jefferson, A., Barrett, T. E., Sheesley, R. J., Ohata, S., Moteki, N., Coe, H., Liu, D., Irwin, M., Tunved, P., Quinn, P. K., and Zhao, Y.: Evaluation of ground-based black carbon measurements by filter-based photometers at two Arctic sites, Journal of Geophysical Research: Atmospheres, 122, 3544–3572, https://doi.org/10.1002/2016JD025843, 2017.

Solomon, A., de Boer, G., Creamean, J. M., McComiskey, A., Shupe, M. D., Maahn, M., and Cox, C.: The relative impact of cloud conden-
885   sation nuclei and ice nucleating particle concentrations on phase partitioning in Arctic mixed-phase stratocumulus clouds, Atmospheric Chemistry and Physics, 18, 17 047–17 059, https://doi.org/10.5194/acp-18-17047-2018, 2018.

Spielhagen, R. F., Werner, K., Sørensen, S. A., Zamelczyk, K., Kandiano, E., Budeus, G., Husum, K., Marchitto, T. M., and Hald, M.: Enhanced Modern Heat Transfer to the Arctic by Warm Atlantic Water, Science, 331, 450–453, https://doi.org/10.1126/science.1197397, 2011.

890   Stein, A. F., Draxler, R. R., Rolph, G. D., Stunder, B. J. B., Cohen, M. D., and Ngan, F.: NOAA's HYSPLIT Atmospheric Transport and Dispersion Modeling System, Bulletin of the American Meteorological Society, 96, 2059 – 2077, https://doi.org/10.1175/BAMS-D-14-00110.1, 2015.

Storelvmo, T.: Aerosol Effects on Climate via Mixed-Phase and Ice Clouds, Annual Review of Earth and Planetary Sciences, 45, 199–222, https://doi.org/10.1146/annurev-earth-060115-012240, 2017.

895   Stroeve, J. C., Serreze, M. C., Holland, M. M., Kay, J. E., Malanik, J., and Barrett, A. P.: The Arctic's rapidly shrinking sea ice cover: a research synthesis, Climatic change, 110, 1005–1027, https://doi.org/https://doi.org/10.1007/s10584-011-0101-1, 2012.

Tan, I. and Storelvmo, T.: Evidence of strong contributions from mixed-phase clouds to Arctic climate change, Geophysical Research Letters, 46, 2894–2902, https://doi.org/https://doi.org/10.1029/2018GL081871, 2019.

Thomas, D. and Charvet, A.: An Introduction to Aerosols, https://doi.org/10.1016/B978-1-78548-215-1.50001-9, 2017.

900   Tobo, Y.: An improved approach for measuring immersion freezing in large droplets over a wide temperature range, Scientific reports, 6, 1–9, https://doi.org/https://doi.org/10.1038/srep32930, 2016.

Tobo, Y., Adachi, K., DeMott, P. J., Hill, T. C., Hamilton, D. S., Mahowald, N. M., Nagatsuka, N., Ohata, S., Uetake, J., Kondo, Y., and Koike, M.: Glacially sourced dust as a potentially significant source of ice nucleating particles, Nature Geoscience, 12, 253–258, https://doi.org/10.1038/s41561-019-0314-x, 2019.

905   Toprak, E. and Schnaiter, M.: Fluorescent biological aerosol particles measured with the Waveband Integrated Bioaerosol Sensor WIBS-4: laboratory tests combined with a one year field study, Atmospheric Chemistry and Physics, 13, 225–243, https://doi.org/10.5194/acp-13-225-2013, 2013.

Vali, G.: Quantitative Evaluation of Experimental Results an the Heterogeneous Freezing Nucleation of Supercooled Liquids, Journal of the Atmospheric Sciences, 28, 402–409, https://doi.org/10.1175/1520-0469(1971)028<0402:QEOERA>2.0.CO;2, 1971.

Vali, G.: Revisiting the differential freezing nucleus spectra derived from drop-freezing experiments: Methods of calculation, applications, and confidence limits, Atmospheric Measurement Techniques, 12, 1219–1231, https://doi.org/10.5194/amt-12-1219-2019, 2019.

Vali, G., DeMott, P. J., Möhler, O., and Whale, T.: A proposal for ice nucleation terminology, Atmospheric Chemistry and Physics, 15, 10 263–10 270, https://doi.org/10.5194/acp-15-10263-2015, 2015.

Vavrus, S.: The Impact of Cloud Feedbacks on Arctic Climate under Greenhouse Forcing, Journal of Climate, 17, 603 – 615, https://doi.org/10.1175/1520-0442(2004)017<0603:TIOCFO>2.0.CO;2, 2004.

Vepuri, H. S. K., Rodriguez, C. A., Georgakopoulos, D. G., Hume, D., Webb, J., Mayer, G. D., and Hiranuma, N.: Ice-nucleating particles in precipitation samples from the Texas Panhandle, Atmospheric Chemistry and Physics, 21, 4503–4520, https://doi.org/10.5194/acp-21-4503-2021, 2021.

Vergara-Temprado, J., Murray, B. J., Wilson, T. W., O'Sullivan, D., Browse, J., Pringle, K. J., Ardon-Dryer, K., Bertram, A. K., Burrows, S. M., Ceburnis, D., DeMott, P. J., Mason, R. H., O'Dowd, C. D., Rinaldi, M., and Carslaw, K. S.: Contribution of feldspar and marine organic aerosols to global ice nucleating particle concentrations, Atmospheric Chemistry and Physics, 17, 3637–3658, https://doi.org/10.5194/acp-17-3637-2017, 2017.

Vergara-Temprado, J., Miltenberger, A. K., Furtado, K., Grosvenor, D. P., Shipway, B. J., Hill, A. A., Wilkinson, J. M., Field, P. R., Murray, B. J., and Carslaw, K. S.: Strong control of Southern Ocean cloud reflectivity by ice-nucleating particles, Proceedings of the National Academy of Sciences, 115, 2687–2692, https://doi.org/10.1073/pnas.1721627115, 2018.

Vignon, E., Alexander, S. P., DeMott, P. J., Sotiropoulou, G., Gerber, F., Hill, T. C. J., Marchand, R., Nenes, A., and Berne, A.: Challenging and Improving the Simulation of Mid-Level Mixed-Phase Clouds Over the High-Latitude Southern Ocean, Journal of Geophysical Research: Atmospheres, 126, e2020JD033 490, https://doi.org/10.1029/2020JD033490, e2020JD033490 2020JD033490, 2021.

Wendisch, M., Macke, A., Ehrlich, A., Lüpkes, C., Mech, M., Chechin, D., Dethloff, K., Velasco, C. B., Bozem, H., Brückner, M., Clemen, H.-C., Crewell, S., Donth, T., Dupuy, R., Ebell, K., Egerer, U., Engelmann, R., Engler, C., Eppers, O., Gehrmann, M., Gong, X., Gottschalk, M., Gourbeyre, C., Griesche, H., Hartmann, J., Hartmann, M., Heinold, B., Herber, A., Herrmann, H., Heygster, G., Hoor, P., Jafariserajehlou, S., Jäkel, E., Järvinen, E., Jourdan, O., Kästner, U., Kecorius, S., Knudsen, E. M., Köllner, F., Kretzschmar, J., Lelli, L., Leroy, D., Maturilli, M., Mei, L., Mertes, S., Mioche, G., Neuber, R., Nicolaus, M., Nomokonova, T., Notholt, J., Palm, M., van Pinxteren, M., Quaas, J., Richter, P., Ruiz-Donoso, E., Schäfer, M., Schmieder, K., Schnaiter, M., Schneider, J., Schwarzenböck, A., Seifert, P., Shupe, M. D., Siebert, H., Spreen, G., Stapf, J., Stratmann, F., Vogl, T., Welti, A., Wex, H., Wiedensohler, A., Zanatta, M., and Zeppenfeld, S.: The Arctic Cloud Puzzle: Using ACLOUD/PASCAL Multiplatform Observations to Unravel the Role of Clouds and Aerosol Particles in Arctic Amplification, Bulletin of the American Meteorological Society, 100, 841 – 871, https://doi.org/10.1175/BAMS-D-18-0072.1, 2019.

Westbrook, C. D. and Illingworth, A. J.: The formation of ice in a long-lived supercooled layer cloud, Quarterly Journal of the Royal Meteorological Society, 139, 2209–2221, https://doi.org/10.1002/qj.2096, 2013.

Wex, H., Huang, L., Zhang, W., Hung, H., Traversi, R., Becagli, S., Sheesley, R. J., Moffett, C. E., Barrett, T. E., Bossi, R., et al.: Annual variability of ice-nucleating particle concentrations at different Arctic locations, Atmospheric Chemistry and Physics, 19, 5293–5311, https://doi.org/https://doi.org/10.5194/acp-19-5293-2019, 2019.

Wieder, J., Mignani, C., Schär, M., Roth, L., Sprenger, M., Henneberger, J., Lohmann, U., Brunner, C., and Kanji, Z. A.: Unveiling atmospheric transport and mixing mechanisms of ice-nucleating particles over the Alps, Atmospheric Chemistry and Physics, 22, 3111–3130, https://doi.org/10.5194/acp-22-3111-2022, 2022.

Wilson, Theodore W., L. L. A., Alpert, P. A., Breckels, M. N., Brooks, I. M., Browse, J., Burrows, S. M., Carslaw, K. S., Huffman, J. A., Judd, C., Kilthau, W. P., Mason, R. H., McFiggans, G., Miller, L. A., Nájera, J. J., Polishchuk, E., Rae, S., Schiller, C. L., Si, M., Temprado, J. V., Whale, T. F., Wong, J. P. S., Wurl, O., Yakobi-Hancock, J. D., Abbatt, J. P. D., Aller, J. Y., Bertram, A. K., Knopf, D. A., and Murray, B. J.: A marine biogenic source of atmospheric ice-nucleating particles, Nature, 525, 234, https://doi.org/10.1038/nature14986, 2015.

Šantl Temkiv, T., Lange, R., Beddows, D., Rauter, U., Pilgaard, S., Dall'Osto, M., Gunde-Cimerman, N., Massling, A., and Wex, H.: Biogenic sources of ice nucleating particles at the high Arctic site villum research station, Environmental science & technology, 53, 10 580–10 590, https://doi.org/https://doi.org/10.1021/acs.est.9b00991, 2019.